Human airway cells prevent SARS-CoV-2 multibasic cleavage site cell culture adaptation

Mart M. Lamers[1], Anna Z. Mykytyn[1], Tim I. Breugem[1], Yiquan Wang[2], Douglas C. Wu[2,3], Samra Riesebosch[1], Petra B. van den Doel[1], Debby Schipper[1], Theo Bestebroer[1], Nicholas C. Wu[2,4,5], Bart L. Haagmans[1]*

[1] Viroscience Department, Erasmus Medical Center, Rotterdam, Netherlands

[2] Department of Biochemistry, University of Illinois at Urbana-Champaign, Urbana, IL 61801, USA

[3] Present address: Invitae Corporation

[4] Center for Biophysics and Quantitative Biology, University of Illinois at Urbana-Champaign, Urbana, IL 61801, USA

[5] Carl R. Woese Institute for Genomic Biology, University of Illinois at Urbana-Champaign, Urbana, IL 61801, USA

* Corresponding author: Bart L. Haagmans

Email: b.haagmans@erasmusmc.nl

Keywords: COVID-19, SARS-CoV-2, cell culture adaptation, multibasic cleavage site, serine proteases, airway organoids, Calu-3, TMPRSS2.

Abstract (116, max 150)

Virus propagation methods generally use transformed cell lines to grow viruses from clinical specimens, which may force viruses to rapidly adapt to cell culture conditions, a process facilitated by high viral mutation rates. Upon propagation in VeroE6 cells, SARS-CoV-2 may mutate or delete the multibasic cleavage site (MBCS) in the spike protein that facilitates serine protease-mediated entry into human airway cells. We report that propagating SARS-CoV-2 on the human airway cell line Calu-3 - that expresses serine proteases - prevents MBCS mutations. Similar results were obtained using a human airway organoid-based culture system for SARS-CoV-2 propagation. Thus, in-depth knowledge on the biology of a virus can be used to establish methods to prevent cell culture adaptation.

Introduction

Severe acute respiratory syndrome coronavirus 2 (SARS-CoV-2) is the causative agent of the ongoing coronavirus disease (COVID-19) pandemic. SARS-CoV-2 emerged late 2019 in China and had spread globally within a few months (Zhu et al., 2020). An unprecedented rapid vaccine development response has led to approval of the first COVID-19 vaccines at the end of 2020. Conversely, the quest for efficacious specific antiviral therapies against SARS-CoV-2 was not successful. The lack of antivirals, the high adaptive capacity of the virus, and the emergence of new strains, indicate that further research on SARS-CoV-2 biology is necessary.

The first step in most SARS-CoV-2 laboratory studies is *in vitro* virus propagation to obtain highly concentrated virus stocks. Despite recent advances in physiologically relevant *in vitro* cell culture systems, methods to propagate clinical isolates have not changed since the first cell lines were established. Traditionally, virus propagation relies on transformed cell lines to produce progeny viruses after inoculation of these cells with a clinical specimen containing the virus. The most widely used cell line in virology is the Vero cell line, which is derived from the kidney of an African green monkey. This cell line and its derivatives (e.g. VeroE6, Vero118, etc) contain genomic deletions of genes involved in the antiviral interferon response (Osada et al., 2014). Such mutations are common in transformed cell lines and allow unbridled virus replication, facilitating the production of high titer virus stocks and allowing research on a wide range of viruses. These isolated viruses are often adapted to their cell culture systems due to their high mutation rates. The development of first and next generation sequencing methods revealed that these adapted viruses were heavily mutated and had drifted significantly from their natural counterparts (Alfson et al., 2018; Lau et al., 2020; Sutter & Moss, 1992; Tamura et al., 2013; H. Wei et al., 2017). Cell culture adaptive mutations often affect viruses phenotypically, both *in vitro* and *in vivo*.

Coronavirus replication is initiated when the viral spike protein binds to the entry receptor on the cell and fuses viral and cellular membranes, allowing the viral RNA to enter the cytoplasm (Hulswit, de Haan, & Bosch, 2016). The spike protein is composed of two domains, the S1 receptor binding domain and the S2 fusion domain, which are separated by the S1/S2 cleavage site. Proteolytic cleavage at the S1/S2 site and the more C-terminal S2' site is required for coronavirus infectivity as this turns on the fusogenic activity of the S2 domain (Millet & Whittaker, 2015). A distinctive feature of SARS-CoV-2 is the presence of a

specific S1/S2 cleavage site in the viral spike protein (Coutard et al., 2020). The SARS-CoV-2 S1/S2 cleavage site contains three basic arginines interrupted by a non-polar alanine (RRAR) and is therefore referred to as a multibasic cleavage site (MBCS). This feature is remarkable as all other viruses within the clade of SARS-related viruses, including SARS-CoV, lack a PRRA insertion that creates this multibasic cleavage site, leading to speculations on whether this site is essential for efficient replication in the human respiratory tract (Hoffmann, Kleine-Weber, & Pohlmann, 2020). Importantly, SARS-CoV-2 isolates that are cultured in the lab rapidly obtain mutations or deletions in the MBCS (Davidson et al., 2020; Klimstra et al., 2020; Lau et al., 2020; Liu et al., 2020; Ogando et al., 2020). On VeroE6 cells, these mutated viruses have a large plaque phenotype, grow to higher titers and outcompete the wildtype virus within 1-4 passages. These mutations have rarely been observed in human clinical specimens (Liu et al., 2020; Wong et al., 2020) and purified MBCS mutants do not efficiently replicate in hamsters (Johnson et al., 2020; Lau et al., 2020). We have recently shown that the MBCS is not required for entry into VeroE6 cells, but is essential for entry into human airway organoids (Mykytyn et al., 2021). We also reported that the MBCS facilitated plasma membrane serine protease-mediated entry, whereas it decreased the dependency on endosomal cathepsins for entry. The serine protease inhibitor camostat mesylate, but not a cathepsin inhibitor, effectively inhibited SARS-CoV-2 entry in human airway organoids, whereas the opposite was observed in VeroE6 cells. These findings demonstrate that SARS-CoV-2 enters relevant airway cells using serine proteases but not cathepsins, and suggest that the multibasic cleavage site is an adaptation to this viral entry strategy. The loss of the MBCS may be an adaptation to the cathepsin-mediated entry pathway present in VeroE6 cells.

97 In this study, we investigated whether mutations in the SARS-CoV-2 spike MBCS could be
98 prevented in a human airway cell line (Calu-3) and 2D air-liquid interface (ALI) airway
99 organoids in which SARS-CoV-2 enters using serine proteases.
100
101 **Results**
102
103 SARS-CoV-2 isolates that are cultured in the lab rapidly lose their spike MBCS (Davidson et
104 al., 2020; Klimstra et al., 2020; Lau et al., 2020; Liu et al., 2020; Ogando et al., 2020).To
105 investigate the extent of cell culture adaptation in our SARS-CoV-2 stocks, we deep-
106 sequenced passage 2, 3 and 4 stocks (P2, P3 and P4) of the BavPat-1 or Munich-1 strain
107 propagated on VeroE6 cells. These stocks were produced from a P1 virus stock grown on
108 VeroE6 cells (Fig S1A). In the P2 stock, the majority of reads (65.3%) in the MBCS were
109 identical to the WT sequence (Fig 1A). In the multibasic RxxR motif both the first (R682L)
110 and the last (R685H) arginine were mutated in 3.5% and 6.1% of reads, respectively. An
111 additional mutation (S686G) directly C-terminal to the MBCS was detected at 25.1%. As this
112 variant increased during passaging and therefore could be an adaptation to cell culture, we
113 included it in our analyses. The P3 stock contained 18.8% wild type (WT) viruses and the
114 S686G was the major MBCS variant at 45.4% while mutations R685H and R682L were
115 present at 22.4% and 7.3%, respectively. A deletion (Del679-688) of the entire MBCS was
116 found as well at 6.1% (Fig 1B). In the P4 virus, the dominant variant contained the R685H
117 mutation at 33.4%, while the Del679-688 and R682L increased to 13.9% and 10.4%,
118 respectively. In the P4 virus, only 9% of reads were WT. Despite the strikingly low level of
119 WT viruses in the VeroE6 stocks, the predominant cleavage motif for the P2 and P3 was still
120 RRARS since mutations never co-occurred (Fig 1A-C). Our results show that a thorough

analysis of deep-sequencing data is required to critically assess culture adaptation. The observations from deep sequencing data were consistent with Sanger sequencing analysis (Fig 1D-F). In agreement with the mixed population of wildtype (WT) and mutant viruses, we observed small (non-adapted) and large (cell culture adapted) plaque phenotypes in a plaque assay for the P2 virus, but plaques increased in size during passaging (Fig 1G).

Whereas the MBCS mutations directly removed arginines (R682L, R685H and the deletion) from the minimal RxxR furin motif, the most common stock mutation was the S686G. This site lies directly C-terminal from the MBCS at positions 682-685, indicating that it may also affect the MBCS functionally. To test this, we assessed the infectivity of the 686 mutation using vesicular stomatitis virus- (VSV) based pseudoviruses expressing a green fluorescent protein (GFP) as described before (Mykytyn et al., 2021). Western blot analysis of cleaved and uncleaved S1 revealed that proteolytic cleavage was observed for the WT SARS-CoV-2 pseudovirus and abrogated by all MBCS mutations tested (del-PRRA, del-RRAR, R682A, R685A and R685H) (Fig 2A, B). For the S686G mutation ~10% cleaved S1 was observed, whereas this was ~80% for WT S (Fig 2A, B). The same difference in cleavage between WT and S686G pseudoviruses was observed for S2 (Fig 2C, D). As expected based on earlier work (Mykytyn et al., 2021), SARS-CoV-2 pseudoviruses with MBCS mutations were more infectious on VeroE6 cells and less infectious on Calu-3 cells (Fig 3A-C). A similar trend was observed for the S686G mutant spike. The infectivity on VeroE6-TMPRSS2 cells was similar for all spikes tested but the WT spike benefited more from TMPRSS2 expression (Fig 3D-E). Protease inhibitors camostat and E64D were then used to block serine proteases and cathepsins, respectively, to assess how spike mutations affect the route of entry. The stable expression of TMPRSS2 in VeroE6 cells leads to entry of WT pseudoviruses via this protease

instead of cathepsin-mediated entry, but SARS-CoV-2 MBCS mutants and to a lesser extent the S686G mutant retained partial cathepsin mediated entry (Fig 3F-I). In addition, a GFP-complementation fusion assay, in which cell-cell fusion occurs at the plasma membrane, showed that MBCS mutations and to a lesser extent the S686G mutation abrogated fusion in VeroE6, VeroE6-TMPRSS2 and Calu-3 cells (Fig 4A-C). These data explain why VeroE6-propagated SARS-CoV-2 stocks rapidly accumulate mutations in the MBCS and at spike position 686. Despite being outside of the MBCS, the S686G mutation impairs spike cleavage, cell-cell fusion and serine protease usage, but not as dramatically as the MBCS mutations or deletions. The low infectivity of MBCS mutants and the S686G mutant on Calu-3 cells indicates that WT viruses could have a selective advantage in these cells.

In order to establish culture conditions in which SARS-CoV-2 is genetically stable, we tested whether WT viruses would have a selective advantage on Calu-3 cells that possess serine protease mediated entry and little cathepsin-mediated entry (Mykytyn et al., 2021). For these experiments we first produced a Calu-3 P2 virus from the VeroE6 P1 stock (Fig 5A). This stock was 100% WT in the MBCS and no major variants (>50%) were detected in the rest of the genome (Fig S5C). An additional round of passaging on Calu-3 cells did not lead to any MBCS mutations, or mutations elsewhere (Fig 5B, Fig S5C). A Calu-3 P3 from a VeroE6 P2 virus did still contain the S686G at low frequency (7.4%) (Fig 5C), but continued passaging to P5 completely removed the S686G (Fig 5D). Again, we did not observe any other major variant mutations in the rest of the genome (Fig S5C). We also produced Calu-3 P4 virus from a VeroE6 P3 stock and we show that while this Calu-3 P4 virus had lost all MBCS mutations, the S686G mutation remained at a frequency of 65.7% (Fig S5A). The addition of E64D to block any cathepsin-mediated entry decreased the frequency of S686G by ~11%, to

54.3%, but did not remove S686G entirely (Fig S5B). These results support our earlier findings (Fig 2; Fig 3; Fig 4) that the S686G is a less severe cell culture adaptation compared with MBCS mutations, and more importantly show that Calu-3 cells can be used to grow genetically stable stocks without MBCS mutations or S686G. Additionally, stocks grown on Calu-3 cells reached titers of 1.47×10^6 - 2.1×10^7 TCID50/ml, indicating that Calu-3 cells support the production of high titer stocks.

To confirm that serine proteases are responsible for the reversal of cell culture adaptation observed in Calu-3 cells, we passaged the adapted VeroE6 P3 stock (Fig 1B) on regular VeroE6 cells or VeroE6-TMPRSS2 cells. P4 viruses grown on VeroE6 cells were only 9% WT and R685H was the dominant variant at 33.4% (Fig 6A; redisplay of Fig 1C). R682L and Del679-688 were present at 10.4% and 13.9%, respectively. Propagation of SARS-CoV-2 in VeroE6-TMPRSS2 cells resulted in an increase in the frequency of wildtype viruses at 21.7% and a decrease in the frequency of MBCS mutations (7.9% R685H; 4.2% R682L; 1.5% Del679-688), but the S686G remained at 64.6% (Fig 6C). The addition of the serine protease inhibitor camostat (10µM) to the VeroE6-TMPRSS2 culture, but not the VeroE6 culture (Fig 6B), increased the frequency of MBCS mutations (36.6% R685H; 13% R682L; 8.8% Del679-688), confirming that serine proteases prevent cell culture adaptation (Fig 6D). As TMPRSS2 expression prevented MBCS mutations, we tested whether the addition of trypsin (0.7µg/ml TPCK-Trypsin) would have a similar effect. Surprisingly, the addition of trypsin to VeroE6 cells, but not VeroE6-TMPRSS2 cells, led to deletion of the entire MBCS (Fig S6A, C). This deletion may arise due to the complete cleavage (S1/S2 and S2') of virus particles that are not bound to the cellular membranes, which would inactivate them. Cell surface expressed TMPRSS2 could accelerate TMPRSS2-mediated entry and cell-cell spread, reducing the

chance of trypsin cleavage in the supernatant. Additionally, we tested whether the addition of fetal bovine serum (FBS, heat-inactivated, 10% final concentration) affected culture adaptation as this is commonly added when producing viral stocks. FBS had a similar effect to trypsin in the VeroE6, but not the VeroE6-TMPRSS2 culture, indicating that proteases capable of cleaving spike may be present in serum and that FBS should be avoided when propagating SARS-CoV-2 (Fig S6B, D).

Next, we hypothesized that the best way to prevent cell culture adaptation would be to propagate the virus in non-transformed human airway cells. Recent advances in stem cell biology have enabled the establishment of human organoid culture systems (Katsura et al., 2020; Nikolic et al., 2017; Sachs et al., 2019; Salahudeen et al., 2020; Sato et al., 2009; Youk et al., 2020). These organoid cultures consist of stem cells that self-renew, allowing prolonged passaging and expansion, but can also differentiate to mature cell types, such as ciliated cells, goblet cells and club cells. Organoids of the airways, the alveoli, and the intestine have recently been used by us to study SARS-CoV-2 entry and pathogenesis (Katsura et al., 2020; Lamers, Beumer, et al., 2020; Lamers, van der Vaart, et al., 2020; Mykytyn et al., 2021; Salahudeen et al., 2020; Youk et al., 2020; Zhou et al., 2020). Pseudoviruses containing MBCS mutations infected human airway organoids poorly (Mykytyn et al., 2021), indicating that these mutations could be prevented by virus propagation in these cells. To produce stocks in human airway organoids, we differentiated the organoids at 2D in transwell inserts at air-liquid interface for twelve weeks as described before (Fig 7A) (Mykytyn et al., 2021). Apical cells, including ciliated cells, in these cultures expressed TMPRSS2 as shown by immunohistochemistry (Fig 7B). To produce viral stocks, 2D airway organoids were inoculated at the apical side at a MOI of 0.05 using the VeroE6 P2

stock (Fig 1A). After a two-hour incubation, cells were washed three times to remove unbound particles. On day two to five post-infection, apical washes were collected and stored at 4°C. During virus collections, bound virus particles were released from cells by pipetting directly on the cell layer. Virus collections from day two and day three (d2+3), and day four and day five (d4+5) were pooled, centrifuged, and filtered to remove debris, dead cells and mucus. In these cultures, ciliated cells were infected, as shown by confocal imaging at day three post infection (Fig 7C). At day five, cultures exhibited widespread infection (Fig 7D) and significant cytopathic effects including loss of ciliated cells (Fig 7D-E) and syncytium formation (Fig 7E). To remove cytokines that could interfere in downstream experiments (such as interferons), we exchanged the medium in the filtered virus collections three times using an Amicon Ultra-15 column (100 kDa cutoff). The resulting titers from the d2+3 and d4+5 stocks were 5.64×10^5 and 1.00×10^7 $TCID_{50}$/ml, respectively, indicating that high titer virus stocks can be made in human airway organoids. Sequencing demonstrated that the high titer organoid stock (d4+5) had a 98.9% WT spike sequence, without multibasic cleavage site mutations and the S686G mutation at only 1.1% (Fig 8A-B). In accordance, the Organoid P3 virus produced small plaques (Fig 8C). No major variants were detected in the rest of the genome (Fig 8D). Next, we investigated S1/S2 cleavage of the VeroE6 P2, P3, Calu-3 P3 and Organoid P3 virus stocks by immunoblot (Fig 8E). The non-adapted Calu-3 and organoid stocks were >85% cleaved, while the VeroE6 P2 and P3 stocks were 71.2% and 33% cleaved, respectively (Figure 8F). The findings support that the Calu-3 and organoid stocks are non-adapted and indicate that *in vivo* the S1/S2 cleavage takes place in the producing cell.

Discussion

241

242 The rapid loss of the SARS-CoV-2 MBCS in cell culture has underlined that some *in vitro*
243 propagation systems may fail to model key aspects of the viral life cycle. As these mutations
244 directly affect the relevance and translatability of all laboratory SARS-CoV-2 experiments, it
245 is pivotal to sort out exactly why these occur in order to prevent them. We and others have
246 previously reported that the SARS-CoV-2 MBCS enhances serine protease-mediated entry,
247 the dominant entry pathway in human airway cells (Hoffmann et al., 2020; Mykytyn et al.,
248 2021). VeroE6 cells, commonly used in the lab to grow virus stocks, lack this entry pathway,
249 forcing the virus to use endosomal cathepsins for entry. This led us to hypothesize that
250 mutations in the MBCS could be prevented in cells with an active serine protease-mediated
251 entry pathway. In this study, we show that the ectopic expression of the serine protease
252 TMPRSS2 in VeroE6 cells prevented MBCS mutations. Virus propagation in Calu-3 cells,
253 which naturally express serine proteases, also prevented cell culture adaptation. Similar
254 results were obtained using a human airway organoid-based culture system for SARS-CoV-2
255 propagation

256

257 Our study shows that SARS-CoV-2 rapidly adapts to VeroE6 cell culture. Therefore, deep-
258 sequencing of viral stocks, which offers a thorough analysis beyond the consensus
259 sequence, is essential. As none of the MBCS mutations co-occurred, consensus sequence
260 logos of culture adapted stocks were often WT, while actually only 10-20% of viral reads
261 contained the WT sequence. Therefore, besides reporting the consensus sequence SARS-
262 CoV-2 studies should preferably also report the percentage of WT reads in the MBCS. The
263 first adaptation to occur in our stocks was the S686G mutation, which lies directly adjacent
264 to the MBCS and decreased Calu-3 infectivity, fusogenicity and S1/S2 cleavage, but not as

265 severely as MBCS mutations. Interestingly, this mutation is rapidly positively selected in
266 ferrets (Richard et al., 2020), and also transmitted, suggesting that there are key differences
267 in transmission between humans and ferrets. Alternatively, it is possible that S686G
268 optimizes cleavage by a specific ferret protease.
269
270 SARS-CoV-2 is generally grown on VeroE6 cells in the presence of 1-10% FBS, as this allows
271 the production of highly concentrated virus stocks. Here, we show that SARS-CoV-2 rapidly
272 acquired mutations in the MBCS upon passaging in VeroE6 cells and that the addition of FBS
273 increases the frequency of MBCS mutations. Currently, we do not know which components
274 of FBS lead to the increased rate of cell culture adaptation, but we hypothesize that (serine)
275 proteases, naturally present in serum (Shimomura, Ochiai, Kondo, & Morimoto, 1992) may
276 be responsible as the addition of trypsin dramatically increased the frequency of MBCS
277 mutations and even led to the deletion of the entire MBCS. The observation that the MBCS
278 is a disadvantage in the presence of trypsin indicates that S2' proteolytic cleavage
279 (performed by trypsin (Hoffmann et al., 2020)) should not occur in the supernatant where it
280 would cause all spikes to shed their S1 and adopt their post fusion conformation prior to
281 encountering the plasma membrane. Alternatively, protease inhibitors in serum
282 (Gstraunthaler, 2003) may block transmembrane serine proteases. For these reasons the
283 use of serum should be avoided when producing virus stocks. The use of defined serum-free
284 media avoids the uncertainty that factors in serum affect the genetic stability of a virus and
285 increase experimental reproducibility due to variations in serum sources.
286
287 We show that the expression of the serine protease TMPRSS2 decreases the replicative
288 fitness of MBCS mutant SARS-CoV-2 viruses, which can then be outcompeted by WT viruses.

289 This indicates that the MBCS is an adaptation to serine proteases and that the serine
290 protease-mediated entry pathway is used for entry *in vivo*. This is in agreement with our
291 earlier observations that SARS-CoV-2 enters using serine proteases on airway organoids
292 (Mykytyn et al., 2021) and that MBCS mutant pseudoviruses could not efficiently infect
293 these cells. Low infectivity of MBCS mutants on the airway cell line Calu-3 was also noted by
294 Hoffmann and colleagues (Hoffmann et al., 2020). In contrast, two CRISPR-based survival
295 screens recently identified several endosomal proteins, including cathepsin L, as essential
296 SARS-CoV-2 genes (Daniloski et al., 2021; J. Wei et al., 2020). As noted recently by Bailey &
297 Diamonds (2020), the identification of endosomal host factors as proviral in cell line-based
298 CRISPR screens requires validation in primary cells (Bailey & Diamond, 2021). Our
299 observation that WT viruses have a selective advantage in 2D airway organoids confirms
300 that the endosomal entry pathway is of little significance in relevant cells.
301
302 As new SARS-CoV-2 strains are emerging now and will continue to emerge for as long as
303 SARS-CoV-2 circulates in humans, there is a need to develop propagation systems that will
304 preserve genetic stability for any given SARS-CoV-2 mutant originating from a human
305 respiratory sample. The closer a culture system mimics the human respiratory tract the less
306 likely it is that a SARS-CoV-2 isolate will adapt. Therefore, we developed a human airway
307 organoid model for SARS-CoV-2 propagation (Figure supplement 8). This model allows high
308 titer SARS-CoV-2 production and was most successful in removing MBCS mutations. In the
309 future we expect that organoid-based systems are likely to replace transformed cell lines
310 when producing viral stocks. The self-renewing capacity of organoids allows labs to share
311 organoid lines, allowing a level of reproducibility similar to that of transformed cell lines.

Organoids can be grown from a wide range of organs and species to best model the *in vivo* environment of a particular virus.

In conclusion, this study shows that SARS-CoV-2 rapidly adapts to VeroE6 cell culture propagation and that this can be prevented by using cell lines with an active serine protease-mediated entry pathway (VeroE6-TMPRSS2 or Calu-3). Alternatively, a 2D airway organoid-based cell culture model can be used for SARS-CoV-2 propagation if in the future new variants emerge that are not genetically stable on Calu-3 cells. Our study also shows that deep-sequencing rather than consensus sequencing of viral stocks is critical for obtaining relevant and reproducible results in SARS-CoV-2 studies.

Materials and Methods

Cell lines

VeroE6 (ATCC® CRL 1586TM) wildtype and retrovirally-transduced cell lines were maintained in Dulbecco's modified Eagle's medium (DMEM, Lonza) supplemented with 10% fetal bovine serum (FBS, Sigma, F7524, heat inactivated for 30 min at 56°C), HEPES, sodium bicabonate, penicillin (100 IU/mL) and streptomycin (100 IU/mL). VeroE6-TMPRSS2, VeroE6-GFP1-10, VeroE6-TMPRSS2-GFP1-10, and Calu-3-GFP1-10 cells were generated as described before (Mykytyn et al., 2021). Calu-3 and Calu-3-GFP1-10 cells were maintained in Eagle's modified Eagle's medium (EMEM, ATCC) supplemented with 10% FBS, penicillin (100 IU/mL) and streptomycin (100 IU/mL). All cell lines were grown at 37°C in a humidified CO2 incubator, and transduced cell lines were cultured in the presence of selection antibiotics.

SARS-CoV-2 propagation in cell lines

SARS-CoV-2 (isolate BetaCoV/Munich/BavPat1/2020; European Virus Archive Global #026V-03883; kindly provided by Dr. C. Drosten) was propagated to the indicated passage on VeroE6, VeroE6-TMPRSS2 or Calu-3 cells, as indicated, in Advanced DMEM/F12 (Gibco), supplemented with HEPES, Glutamax, penicillin (100 IU/mL) and streptomycin (100 IU/mL) (AdDF+++) at 37°C in a humidified CO2 incubator. Infections were performed at a multiplicity of infection (MOI) of 0.01 and virus was harvested after 72 hours. The culture supernatant was cleared by centrifugation and stored at −80°C. Calu-3 stocks were additionally cleared using a 0.45 µM low protein binding filter (Millipore) to remove mucus debris produced by these cells and the medium was exchanged three times for Opti-MEM I (1X) + GlutaMAX (Gibco) using an Amicon Ultra-15 column (100 kDa cutoff). At the end of each centrifugation step approximately 2 ml was left in the top compartment. After three exchanges the purified virus was transferred to a new 50 ml tube and the Amicon Ultra-15 column was washed ten times by adding 1 ml Opti-MEM I (1X) + GlutaMAX (Gibco) to the top compartment, pipetting up and down several times on the filter and adding each wash to the tube containing the purified virus preparation. This step was repeated until the volume in the purified virus stock was equal to the original volume of culture supernatant. Purified virus was stored at -80°C in aliquots. Stock titers were determined by preparing 10-fold serial dilutions in Opti-MEM I (1X) + GlutaMAX (Gibco). One-hundred µl of each dilution was added to monolayers of 2×10^4 VeroE6 cells in the same medium in a 96-well plate. Plates were incubated at 37°C for 5 days and then examined for cytopathic effect. The TCID50 was calculated according to the method of Spearman & Kärber. All work with infectious SARS-CoV-2 was performed in a Class II Biosafety Cabinet under BSL-3 conditions at Erasmus Medical Center.

360

361 *Cloning*

362 Cloning of SARS-CoV-2 S WT, del-PRRA, R685A and R685H constructs for pseudovirus
363 production and GFP-complementation fusion assay was performed as described before
364 (Mykytyn et al., 2021). Del-RRAR, R682A and S686G plasmids were generated by
365 mutagenesis PCR.

366

367 *Organoid culture and differentiation*

368 Human airway stem cells were isolated and grown into organoids, and passaged as
369 described before (Lamers, Beumer, et al., 2020) using a protocol adapted from Sachs and
370 colleagues (2019). Adult lung tissue was obtained from residual, tumor-free, material
371 obtained at lung resection surgery for lung cancer. The Medical Ethical Committee of the
372 Erasmus MC Rotterdam granted permission for this study (METC 2012-512). Study
373 procedures were performed according to the Declaration of Helsinki, and in compliance
374 with relevant Dutch laws and institutional guidelines. The tissues obtained were
375 anonymized and non-traceable to the donor. In this study we used organoids from one
376 donor, from which bronchial and bronchiolar organoids were grown. Differentiation of
377 human airway organoids at air-liquid interface was performed as described before (Lamers,
378 Beumer, et al., 2020). Cultures were differentiated for 8-12 weeks at air-liquid interface.

379

380 *SARS-CoV-2 stock production on 2D air-liquid interface human airway organoids*

381 To produce stocks in human airway organoids, we differentiated the bronchial organoids in
382 transwell inserts at air-liquid interface for twelve weeks. A total of twelve 12 mm transwell
383 inserts were washed three times in AdDF+++ before inoculation at the apical side at a MOI

of 0.05. After a two-hour incubation, cells were washed three times with AdDF+++ to remove unbound particles. Twenty-four hours post-infection, cells were washed by adding 500 ul AdDF+++ to the apical side of the cells and incubating at 37°C 5% CO2 for 30 min to disperse the newly produced virus particles, facilitating the next round of infection. Next, the medium was removed and discarded, as generally little virus is produced in the first 24 hours (Lamers et al., 2020). At day two to five post-infection, washes were collected and stored at 4°C. During collections bound virus particles were removed from the cells by pipetting three times directly on the cell layer after the 30 min incubation step at 37°C 5% CO2. Virus collections from day two and day three (d2+3), and day four and day five (d4+5) were pooled, mixed by pipetting, centrifuged at 4000 x g for 4 min, and filtered through a 0.45um low protein binding filter (Millipore) to remove debris, dead cells and mucus. To remove cytokines that could interfere in downstream experiments (such as interferons), we exchanged the medium in the filtered virus collections three times with Opti-MEM I (1X) + GlutaMAX (Gibco) using an Amicon Ultra-15 column (100 kDa cutoff). At the end of each centrifugation step approximately 2 ml was left in the top compartment. After three exchanges, the purified virus was transferred to a new 50 ml tube and the Amicon Ultra-15 column was washed ten times by adding 1 ml Opti-MEM I (1X) + GlutaMAX (Gibco) to the top compartment, pipetting up and down several times on the filter and adding each wash to the tube containing the purified virus preparation, resulting in a total volume of ~12 ml. Next, virus preparations were aliquoted in 500 µl aliquots, stored at -80°C and thawed for titrations on VeroE6 cells.

Pseudovirus assay

Pseudovirus production, infectivity and entry assays were performed as described before (Mykytyn et al., 2021). Briefly, pseudoviruses expressing WT, MBCS mutant and S686G S were titrated by preparing 10-fold serial dilutions in Opti-MEM I (1X) + GlutaMAX (Gibco). Thirty µl of each dilution was added to monolayers of 2×10^4 VeroE6, VeroE6-TMPRSS2 or 8×10^4 Calu-3 cells in the same medium in a 96-well plate. Titrations were performed in triplicate. Plates were incubated at 37°C overnight and then scanned on the Amersham Typhoon Biomolecular Imager (channel Cy2; resolution 10 µm; GE Healthcare). Entry routes were determined by pre-treating monolayers of VeroE6 or VeroE6-TMPRSS2 cells with a concentration range of camostat mesylate (Sigma) or E64D (MedChemExpress) diluted in Opti-MEM I (1X) + GlutaMAX (Gibco) for 2 hours prior to infection with 1×10^3 pseudovirus. Plates were incubated at 37°C overnight and then scanned on the Amersham Typhoon Biomolecular Imager (channel Cy2; resolution 10 mm; GE Healthcare). All pseudovirus experiments were quantified using ImageQuant TL 8.2 image analysis software (GE Healthcare).

Pseudovirus concentration

Pseudoviruses were concentrated as described before (Mykytyn et al., 2021) on a 10% sucrose cushion (10% sucrose, 15 mM Tris–HCl, 100 mM NaCl, 0.5 mM EDTA) for 1.5 hours at 20,000 x g at 4°C. Supernatant was decanted and pseudoviruses resuspended in Opti-MEM I (1X) + GlutaMAX (Gibco) to achieve 100-fold concentration.

Immunoblotting

Concentrated pseudovirus stocks were diluted to a final concentration of 1x Laemmli loading buffer (Bio-Rad) containing 5% 2-mercaptoethanol. Authentic viruses were diluted

to a final concentration of 2x Laemmli loading buffer containing 5% 2-mercaptoethanol. All samples were boiled for 30 minutes at 95°C. Samples were used for SDS-PAGE analysis using precast 10% TGX gels (Bio-Rad). Gels were run in tris-glycine SDS (TGS) buffer at 50V for 30 minutes and subsequently at 120V for 90 minutes. Transfer was performed at 300mA for 55 minutes onto 0.45 µm Immobilon-FL PVDF membranes in TGS containing 20% methanol. Spike was stained using polyclonal rabbit-anti-SARS-CoV S1 (1:1000, Sino Biological), mouse-anti-SARS-CoV-2 S2 (1:1000, Genetex), SARS-CoV-2 nucleoprotein was stained using rabbit-anti-SARS-CoV NP (1:1000, Sino Biological) and VSV nucleoprotein was stained using mouse-anti-VSV-N (1:1000, Absolute Antibody) followed by infrared-labelled secondary antibodies (1:20,000; Licor). Western blots were scanned on an Odyssey CLx and analyzed using Image Studio Lite Ver 5.2 software.

GFP-complementation fusion assay

Fusion assays were performed as described before (Mykytyn et al., 2021). Briefly, HEK-293T cells were transfected with 1.5 µg pGAGGS-spike (all coronavirus S variants described above) DNA and pGAGGS-β-Actin-P2A-7xGFP11-BFP DNA or empty vector DNA with PEI in a ratio of 1:3 (DNA : PEI). Transfected HEK-293T cells were incubated overnight at 37°C 5% CO_2, resuspended in PBS and added to GFP1-10 expressing VeroE6, VeroE6-TMPRSS2 and Calu-3 cells in Opti-MEM I (1X) + GlutaMAX at a ratio of 1:80 (HEK-293T cells : GFP1-10 expressing cells). Fusion events were quantified by detecting GFP+ pixels after 18 hours incubation at 37°C 5% CO_2 using Amersham™ Typhoon™ Biomolecular Imager (channel Cy2; resolution 10µm; GE Healthcare). Data was analyzed using the ImageQuant TL 8.2 image analysis software (GE Healthcare) by calculating the sum of all GFP+ pixels per well.

455 *Plaque assay*

456 Virus stock were diluted in 10-fold serial dilutions in 2ml Opti-MEM I (1X) + GlutaMAX
457 (Gibco). 1 ml of each dilution was added to monolayers of 2×10^6 VeroE6 cells in the same
458 medium in a 6-well plate. Cells were incubated at 37°C for one hour and then overlaid with
459 1.2% Avicel (FMC biopolymers) in Opti-MEM I (1X) + GlutaMAX (Gibco) for 72 hours. Next,
460 they were washed once in PBS, fixed in formalin, permeabilized in 70% ethanol and washed
461 in PBS again. Cells were blocked in 3% BSA (bovine serum albumin; Sigma) in PBS, stained
462 with mouse anti-nucleocapsid (Sino biological; 1:1000) in PBS containing 0.1% BSA, washed
463 three times in PBS, then stained with goat anti-mouse Alexa Fluor 488 (Invitrogen; 1:2000)
464 in PBS containing 0.1% BSA and then washed three times in PBS. All staining steps were
465 performed at room temperature for one hour. Plates were scanned on the Amersham
466 Typhoon Biomolecular Imager (channel Cy2; resolution 10 µm; GE Healthcare).

467

468 *Sanger sequencing*

469 To sequence spike gene fragments, RNA was extracted as described above and used for
470 cDNA synthesis using Superscript IV (Invitrogen), according to the manufacturer's
471 instructions. PCR was performed using PfuUltra II Fusion HS DNA Polymerase (Agilent
472 Technologies) and primers 5'-TGACACTACTGATGCTGTCCGTG-3' and 5'-
473 GATGGATCTGGTAATATTTGTG-3' under the following conditions: initial denaturation at 95°C
474 for 3 min, followed by 25 cycles of (95°C for 20 s, 52°C for 20 s, and 72°C for 60 s), and a final
475 extension at 72°C for 10 min. The amplicons were purified (Qiagen PCR purification kit,
476 according to manufacturer) and sequenced with the forward primer using the BigDye
477 Terminator v3.1 Cycle Sequencing Kit and an ABI PRISM 3100 genetic analyzer (Applied

478 Biosystems). The obtained sequences were assembled and aligned using Benchling (MAFFT
479 algorithm).
480
481
482 *Fixed immunofluorescence microscopy and immunohistochemistry*
483 Transwell inserts were fixed in formalin, permeabilized in 0.1% Triton X-100, and blocked for
484 60 minutes in 10% normal goat serum in PBS (blocking buffer). Cells were incubated with
485 primary antibodies overnight at 4°C in blocking buffer, washed twice with PBS, incubated
486 with corresponding secondary antibodies Alexa488-, 594-conjugated secondary antibodies
487 (1:400; Invitrogen) in blocking buffer for two hours at room temperature, washed two times
488 with PBS, incubated for 10 minutes with Hoechst, washed twice with PBS, and mounted in
489 Prolong Antifade (Invitrogen) mounting medium. SARS-CoV-2 was stained with rabbit-anti-
490 SARS-CoV nucleoprotein (40143-T62, 1:1000, Sino biological). Ciliated cells were stained
491 with mouse-anti-AcTub (sc-23950 AF488, 1:100, Santa Cruz Biotechnology). For TMPRSS2
492 stainings formalin-fixed inserts were paraffin-embedded, sectioned and deparaffinized as
493 described before prior to staining (Rockx et al., 2020). Samples were imaged on a LSM700
494 confocal microscope using ZEN software (Zeiss). Immunohistochemistry was performed as
495 described previously (Rockx et al., 2020) on formalin fixed, paraffin embedded Transwell
496 inserts. TMPRSS2 was stained using mouse-anti-TMPRSS2 (sc-515727, 1:200, Santa Cruz
497 Biotechnology), and visualized with goat-anti-mouse (PO260, 1:100, Dako) horseradish
498 peroxidase labeled secondary antibody, respectively. Samples were counterstained using
499 haematoxylin.
500
501 *Illumina sequencing*

For deep- sequencing, RNA was extracted as described above and subsequently cDNA was generated using ProtoscriptII reverse transcriptase enzyme (New England BiotechnologieBioLabs) according to the manufacturer's protocol. A SARS-CoV-2 specific multiplex PCR was performed as recently described (Oude Munnink et al., 2020). In short, primers for 86 overlapping amplicons spanning the entire genome were designed using primal scheme (http://primal.zibraproject.org/.). The amplicon length was set to 500 bp with 75 bp overlap between the different amplicons. Amplicons were purified with 0.8x AMPure XP beads (Beckman Coulter) and 100 ng of DNA was converted into paired-end Illumina sequencing libraries using KAPA HyperPlus library preparation kit (Roche) with the KAPA unique dual-indexed adapters (Roche), following the manufacturer's recommendations. The barcode-labeled samples were pooled and analyzed on an Illumina sequencer V3 MiSeq flowcell (2×300 cycles).

Sequencing data analysis

Adapters from the paired-end sequencing reads were trimmed using cutadapt (https://doi.org/10.14806/ej.17.1.200) via: cutadapt -B AGATCGGAAGAGCGTCGTGTAGGGAAAGAGTG -b AGATCGGAAGAGCACACGTCTGAACTCCAGTCAC --interleaved --minimum-length 50. The trimmed reads were aligned to the genome of Bavpat-1 with Bowtie2 (PMC3322381) using parameters: --no-discordant --dovetail --no-mixed --maxins 2000. Primer sequences were trimmed off from the alignments by soft-clipping the leftmost 33 bases from each sequencing reads using BamUtil (PMC4448687) via: trimbam {bam_file} - -L 30 -R 0 --clip. Variants calling was done using VarScan2 (PMC3290792) and SAMtools (PMC2723002) via: samtools mpileup --excl-flags 2048 --excl-flags 256 --fasta-ref {REFERENCE_FAASTA} --max-

526 depth 50000 --min-MQ 30 --min-BQ 30 {BAM_FILE} | varscan pileup2cns --min-coverage 10
527 --min-reads2 2 --min-var-freq 0.01 --min-freq-for-hom 0.75 --p-value 0.05 --variants 1 >
528 {snp_file}. Sequence logo were generated with logomaker (PMC7141850) using a custom
529 python script. Plotting of mutation frequencies was done using R and ggplot2 (Hadley,
530 2016). All scripts used for data processing are deposited in GitHub:
531 https://github.com/wchnicholas/SARS_CoV2_mutation. Raw sequencing data will be
532 submitted to the NIH Short Read Archive under accession number: BioProject PRJNA694097.
533
534 *Statistics*
535 Statistical analysis was performed with the GraphPad Prism 8 and 9 software using an
536 ANOVA or two-way ANOVA followed by a Bonferroni multiple-comparison test.
537
538

Key Resources Table				
Reagent type (species) or resource	**Designation**	**Source or reference**	**Identifiers**	**Additional information**
VeroE6 (*Cercopithecus aethiops*)	Monkey kidney cell line	ATCC	CRL 1586TM	
Calu-3 (*Homo sapien*)	Lung adenocarcinoma cell line	ATCC	HTB 55	

VeroE6 TMPRSS2	Monkey kidney cell line	Mykytyn et al. 2020	Mykytyn et al. 2020	
VeroE6 GFP1-10	Monkey kidney cell line	Mykytyn et al. 2020	Mykytyn et al. 2020	
VeroE6 GFP1-10 TMPRSS2	Monkey kidney cell line	Mykytyn et al. 2020	Mykytyn et al. 2020	
Calu-3 GFP1-10	Lung adenocarcinoma cell line	Mykytyn et al. 2020	Mykytyn et al. 2020	
SARS-CoV-2 BavPat1/Munich-1	SARS-CoV-2	Dr. Christian Drosten	European Virus Archive Global #026V-03883	
Airway tissue for organoids (*Homo sapien*)	Airway organoids	Mykytyn et al. 2020	Mykytyn et al. 2020	
Aloxistatin	E64D	MedChemExpress	Cat# HY-100229	
Camostat mesylate	Camostat	Sigma	Cat# SML0057	
Polyethylenimine linear	Polyethylenimine	Polysciences	Cat# 23966	

Hygromycin B	Hygromycin B	Invitrogen	Cat# 10843555001	
G418, Geneticin	Geneticin	Invitrogen	Cat# 10131035	
Avicel	Avicel	FMC biopolymers	-	
Amicon Ultra-15 Centrifugal Filter Unit with Ultracel-100 membrane	Amicon Ultra-15 Centrifugal Filter Unit with Ultracel-100 membrane	Millipore	Cat# UFC910024	
Opti-MEM I (1X) + GlutaMAX	Opti-MEM I (1X) + GlutaMAX	Gibco	Cat# 51985-042	
Advanced DMEM/F12	Advanced DMEM/F12	Thermo Fisher scientific	Cat# 12634-010	
AO medium	AO medium	Sachs et al. 2019	N/A	
Pneumacult ALI medium	Pneumacult ALI medium	Stemcell	Cat # 05001	
TryplE	TryplE	Thermo Fisher scientific	Cat# 12605010	

Cultrex Basement Membrane Extract, Type 2	Basement membrane extract	R&D Systems	Cat# 3533-005-02	
12 mm Transwell® with 0.4 µm Pore Polyester Membrane Insert, Sterile	Transwell inserts	Corning	Cat# 3460	
Collagen Type I, High concentration Rat tail	Collagen	Corning	Cat# 354249	
0.45µm low protein binding filter	0.45µm low protein binding filter	Millipore	Cat# SLHV033RS	
Antibody	Rabbit-anti-SARS-CoV NP (polyclonal)	Sino Biological	Cat# 40143-T62	IF (1:1000)
Antibody	Mouse anti-TMPRSS2 (monoclonal)	Santa Cruz	Cat# sc-515727	IHC (1:200)

Antibody	Goat-anti-mouse	Dako	Cat# P0260	IF (1:400)
Antibody	Goat anti-rabbit IgG (H+L) Alexa Fluor Plus 594	Invitrogen	Cat# A32740	IF (1:400)
Antibody	Goat anti-mouse IgG (H+L) Alexa Fluor 488	Invitrogen	Cat# A11029	IF (1:2000)
Antibody	Mouse-anti-AcTub IgG2A Alexa Fluor 488 (monoclonal)	Santa Cruz Biotechnology	Cat# sc-23950 AF488	IF (1:100)
Antibody	mouse anti-nucleocapsid	Sinobiological	Cat# 40143-MM05	IF (1:1000)
Antibody	Rabbit anti-SARS-CoV S1 (polyclonal)	Sinobiological	Cat# 40150-T62	WB (1:1000)
Antibody	Mouse-anti-SARS-CoV-2 S2 (monoclonal)	Genetex	Cat# GTX632604	WB (1:1000)

Antibody	Mouse-anti-VSV-N (monoclonal)	Absolute Antibody	Cat# Ab01403-2.0	WB (1:1000)
Hoechst 33342, Trihydrochloride, Trihydrate	Hoechst	Thermo Fisher	Cat# H1399	
4x Laemmli Sample Buffer	Laemmli	BioRad	Cat# 1610747	
SuperScript™ IV Reverse Transcriptase	SuperScript™ IV Reverse Transcriptase	Invitrogen	Cat# 18090200	
pfu ultra II fusion HS DNA polymerase	Pfu Ultra II Fusion HS DNA Polymerase	Agilent Technologies	Cat# 600674	
Qiaquick PCR Purification Kit	Qiaquick PCR Purification Kit	QIAGEN	Cat# 28104	
BigDye™ Terminator v3.1 Cycle Sequencing Kit	BigDye™ Terminator v3.1 Cycle Sequencing Kit	Applied Biosystems	Cat# 4337456	

ProtoScript II Reverse Transcriptase	ProtoScript II Reverse Transcriptase	New England BioLabs	Cat# NEB M0368X	
Ampure XP Beads	Ampure XP Beads	Beckman Coulter	Cat# A63882	
KAPA HyperPlus	KAPA HyperPlus	Roche	Cat# 7962428001	
Illumina sequencer V3 MiSeq flowcell	Illumina sequencer V3 MiSeq flowcell	Illumina		
ABI PRISM® 3100 Genetic Analyzer	ABI PRISM® 3100 Genetic Analyzer	Applied Biosystems		
Odyssey CLx	Odyssey CLx	Licor		
Amersham™ Typhoon™ Biomolecular Imager	Amersham™ Typhoon™ Biomolecular Image	GE Healthcare		
Amersham™ Imager 600	Amersham™ Imager 600	GE Healthcare		
LSM700 confocal microscope	LSM700 confocal microscope	Zeiss		

Carl ZEISS Vert.A1	Carl ZEISS Vert.A1	Zeiss		
ZEN software	ZEN	Zeiss		
ImageQuant TL 8.2	ImageQuant TL 8.2	GE Healthcare		
Studio Lite Ver 5.2	Studio Lite Ver 5.2	Licor		
GraphPad PRISM 8, 9	GraphPad PRISM 8, 9	GraphPad		
Adobe Illustrator	Illustrator	Adobe inc.		

Acknowledgments

This work was supported by the Netherlands Organization for Health Research and Development (ZONMW) grant agreement 10150062010008 to B.L.H and co-funded by the PPP Allowance (grant agreement LSHM19136) made available by Health Holland, Top Sector Life Sciences & Health, to stimulate public-private partnerships. The present manuscript was part of the research program of the Netherlands Centre for One Health. The funders had no role in study design, data collection and interpretation, or the decision to submit the work for publication

Competing interests

550 The authors declare that no competing interests exist.

551

552 **Figure Legends**

553

554 **Figure 1. SARS-CoV-2 rapidly acquires multibasic cleavage site mutations when**
555 **propagated on VeroE6 cells.** (**A-C**) Deep-sequencing analysis of VeroE6 passage 2 (**A**),
556 passage 3 (**B**) and passage 4 (**C**) virus stocks. In each graph the amino acid sequence logo of
557 the multibasic cleavage site is shown. (**D-F**) Sanger sequencing chromatograms of VeroE6
558 passage 2 (**D**), passage 3 (**E**), and passage 4 (**F**) viruses. Multibasic cleavage site mutations
559 identified by deep-sequencing are indicated with arrows. Translated sequences are
560 indicated below Sanger reads. (**G**) Plaque size analysis of VeroE6 passage 2-4 virus stocks on
561 VeroE6 cells. Red arrow heads indicate small plaques.

562

563 **Figure 2. Mutations in the multibasic cleavage site and the adjacent serine residue (S686)**
564 **abrogate S1/S2 cleavage.** (**A**) Analysis of S1/S2 cleavage by S1 immunoblot of SARS-CoV-2 S
565 (WT), multibasic cleavage site (MBCS) mutant and S686G mutant pseudoviruses. (**B**)
566 Quantification of S1 cleavage from four independent pseudovirus productions. (**C**) Analysis
567 of S1/S2 cleavage by multiplex S1 (red) and S2 (green) immunoblot of SARS-CoV-2 S (WT)
568 and S686G mutant pseudoviruses. S0 indicates uncleaved spike; S1 indicates the S1 domain
569 of cleaved spike; VSV-N indicates VSV nucleoprotein (production control). Numbers indicate
570 the molecular weight (kDa) of bands of the protein standard. (**D**) Quantification of S2
571 cleavage from four independent pseudovirus productions. Error bars indicate SD. EV =
572 empty vector. WT = wild type. kDa = kilo dalton.

573 **Figure 3. The SARS-CoV-2 multibasic cleavage site and the adjacent serine residue (S686)**
574 **enhance infectivity and serine protease mediated entry on Calu-3 and VeroE6-TMPRSS2**
575 **cells.** (**A-B**) SARS-CoV-2 (WT), multibasic cleavage site (MBCS) mutant and S686G
576 pseudovirus infectious titers on (**A**) VeroE6 and (**B**) Calu-3 cells. (**C**) Fold change in SARS-CoV-
577 2, MBCS mutant and S686G pseudovirus infectious titers on Calu-3 cells over infectious
578 titers on VeroE6 cells. (**D**) SARS-CoV-2, MBCS mutant and S686G pseudovirus infectious
579 titers on VeroE6-TMPRSS2 cells. (**E**) Fold change in SARS-CoV-2, MBCS mutant and S686G
580 pseudovirus infectious titers on VeroE6-TMPRSS2 cells over infectious titers on VeroE6 cells.
581 One-way ANOVA was performed for statistical analysis comparing all groups with WT. (**F-I**)
582 SARS-CoV-2, MBCS mutant and S686G pseudovirus entry into (**F and G**) VeroE6 cells or (**H**
583 **and I**) VeroE6-TMPRSS2 cells pre-treated with a concentration range of either (**F and H**)
584 camostat mesylate or (**G and I**) E64D. Two-way ANOVA, followed by a bonferroni post hoc
585 test was performed for statistical analysis comparing all groups to WT. WT pseudovirus
586 entry into VeroE6 cells treated with 10µM E64D was significantly different from del-RRAR,
587 R682A, R685A and S686G pseudovirus entry. * indicates statistical significance ($p<0.05$)
588 compared to WT (A-E). * indicates statistical significance ($p<0.05$) compared to WT at the
589 highest inhibitor concentration (**F-I**). Experiments were performed in triplicate.
590 Representative experiments from at least two independent experiments are shown. Error
591 bars indicate SD. WT = wild type.
592
593 **Figure 4. Multibasic cleavage site mutations and the adjacent serine residue (S686) impair**
594 **spike protein fusogenicity.** (**A-C**) Fusogenicity of wild type SARS-CoV-2 spike and spike
595 mutants was assessed after 18 hours by measuring the sum of all GFP+ pixels per well in a
596 GFP-complementation fusion assay on VeroE6-GFP1-10 (**A**), VeroE6-TMPRSS2-GFP1-10 (**B**),

and Calu-3-GFP1-10 (**C**) cells. The experiment was performed in triplicate. A representative experiment from two independent experiments is shown. Statistical analysis was performed by one-way ANOVA. * indicates a significant difference compared to WT ($P<0.05$). Error bars indicate SD. EV = empty vector. WT = wild type.

Figure 5. SARS-CoV-2 propagation in Calu-3 cells efficiently prevents SARS-CoV-2 cell culture adaptation. (**A**) Deep-sequencing analysis of Calu-3 passage 2 virus from a VeroE6 passage 1. (**B**) Deep-sequencing analysis of Calu-3 passage 3 virus from the Calu-3 passage 2 in A. (**C**) Deep-sequencing analysis of Calu-3 passage 3 virus grown from a VeroE6 passage 2 stock (Figure 1A). Deep-sequencing analysis of Calu-3 passage 5 virus from a Calu-3 passage 3 stock in C. In each graph the amino acid sequence logo of the multibasic cleavage site is shown.

Figure 6. Serine protease expression prevents MBCS mutations. (**A-B**) Deep-sequencing analysis of VeroE6 passage 4 virus from a VeroE6 passage 3 (A is a redisplay of Figure 1C) mock-treated or treated with 10µM camostat. (**C-D**) Deep-sequencing analysis of VeroE6-TMPRSS2 passage 4 virus from a VeroE6 passage 3 mock-treated or treated with 10µM camostat. In each graph the amino acid sequence logo of the multibasic cleavage site is shown.

Figure 7. A 2D air-liquid interface human airway organoid model for SARS-CoV-2 propagation. (**A**) Human airway organoids were dissociated and plated onto 12 mm transwell inserts. After an 8-12 week differentiation period at air-liquid interface cultures contained ciliated, non-ciliated and basal cells as shown on a hematoxylin-eosin stain. (**B**)

621 Air-exposed cells, but not basal cells, expressed the priming protease TMPRSS2 as shown by
622 immunohistochemistry. (**C**) Immunofluorescent staining indicated that in these cultures,
623 ciliated cells (acetylated tubulin+ or AcTUB+ cells) were infected by SARS-CoV-2. (**D and E**) At
624 5 days post-infection, whole-well confocal imaging indicated the infection was widespread
625 (**D**) and cytopathic effects, including cilia damage (**D and E**) and syncytial cells (**E**) were
626 visible. Scale bars indicate 20µm in A, B, C; 2mm in D; and 100µm in E.
627
628 **Figure 8. 2D air-liquid interface human airway organoids produce high titer stocks without**
629 **multibasic cleavage site mutations.** (**A-B**) Deep-sequencing analysis (**A**) and Sanger
630 chromatogram (**B**) of Organoid passage 3 virus from a VeroE6 passage 2 stock (Figure 1A).
631 The amino acid sequence logo of the multibasic cleavage site is shown. The translated
632 sequence is indicated below the Sanger read. Arrows indicate where cell culture adaptations
633 to VeroE6 cells occur. (**C**) Plaque size analysis of VeroE6 passage 2 and Organoid passage 3
634 virus (the VeroE6 data is a redisplay of Figure 1G). Red arrow heads indicate large plaques.
635 (**D**) Full genome deep-sequencing analysis of VeroE6 passage 2 and organoid passage 3
636 stocks. In D VeroE6 P2 is a redisplay of VeroE6 P2 in Figure supplement 1B. (**E**) Immunoblot
637 analysis of VeroE6 passage 2 and 3, Calu-3 passage 3 and Organoid passage 3 stocks. S0
638 indicates uncleaved spike; S1 indicates the S1 domain of cleaved spike; NP indicates
639 nucleoprotein. Numbers indicate the molecular weight (kDa) of bands of the protein
640 standard. (**F**) Quantification of cleavage from three immunoblots. Error bars indicate SD.
641 kDa = kilo dalton.
642
643 **Figure supplement 1. Deep-sequencing analysis of VeroE6 passage 1 virus multibasic**
644 **cleavage site and full genome deep-sequencing analysis of passage 1-4 viruses.** (**A**) Deep-

sequencing analysis of the VeroE6 passage 1 virus stock. In each graph the amino acid sequence logo of the multibasic cleavage site is shown. (**B**) Full genome deep-sequencing analysis of VeroE6 passage 1, 2, 3 and passage 4 viruses.

Figure supplement 5. Multibasic cleavage site deep-sequencing analysis of passage 4 Calu-3 viruses from an adapted VeroE6 P3 stock and full genome deep-sequencing analysis of Calu-3 propagated viruses. (**A**) Deep-sequencing analysis of Calu-3 passage 4 virus from a VeroE6 passage 3 stock (from Figure 1B). (**B**) Deep-sequencing analysis of Calu-3 passage 4 virus from a VeroE6 passage 3 stock produced in the presence of 10µM E64D. In each graph the amino acid sequence logo of the multibasic cleavage site is shown. (**C**) Full genome deep-sequencing analysis of Calu-3 propagated viruses.

Figure supplement 6. Multibasic cleavage site and full genome deep-sequencing analysis of passage 4 VeroE6 and VeroE6-TMPRSS2 viruses. (**A-B**) Deep-sequencing analysis of VeroE6 passage 4 virus from a VeroE6 passage 3, trypsin-treated (**A**) or treated with 10% FBS (**B**). (**C-D**) Deep-sequencing analysis of VeroE6-TMPRSS2 passage 4 virus from a VeroE6 passage 3, trypsin-treated (**C**) or treated with 10% FBS (**D**). In each graph the amino acid sequence logo of the multibasic cleavage site is shown. (**E**) Full genome deep-sequencing analysis of VeroE6 and VeroE6-TMPRSS2 propagated viruses. In E VeroE6 P4 (mock) is a redisplay of VeroE6 P4 in Figure supplement 1B.

Figure supplement 8. Schematic workflow for the production of SARS-CoV-2 stocks on 2D air-liquid interface differentiated airway organoids. Step 1. 3D self-renewing airway organoids are grown from human lung tissue. Next, these are dissociated to single cells and

669 differentiated at air-liquid interface for 4-12 weeks. Step 2. Differentiated cultures are
670 infected at a multiplicity of infection of 0.05 and washed daily for 5 days. The washes from
671 day 2-5 are collected and stored at 4°C. Step 3. Virus collections are cleared by
672 centrifugation and filtered to remove debris larger than 0.45 µm. Next, the medium is
673 exchanged three times using Amicon columns to remove cytokines and debris smaller than
674 100 kDa. Purified virus preparations are then stored at -80°C in aliquots. Step 4. Stocks can
675 be characterized using plaque assays, Sanger sequencing and deep-sequencing. Created
676 with BioRender.com.

677

678 **References**

679

680 Alfson, K. J., Avena, L. E., Delgado, J., Beadles, M. W., Patterson, J. L., Carrion, R., Jr., &
681 Griffiths, A. (2018). A Single Amino Acid Change in the Marburg Virus Glycoprotein
682 Arises during Serial Cell Culture Passages and Attenuates the Virus in a Macaque
683 Model of Disease. *mSphere, 3*(1). doi:10.1128/mSphere.00401-17
684 Bailey, A. L., & Diamond, M. S. (2021). A Crisp(r) New Perspective on SARS-CoV-2 Biology.
685 *Cell, 184*(1), 15-17. doi:10.1016/j.cell.2020.12.003
686 Coutard, B., Valle, C., de Lamballerie, X., Canard, B., Seidah, N. G., & Decroly, E. (2020). The
687 spike glycoprotein of the new coronavirus 2019-nCoV contains a furin-like cleavage
688 site absent in CoV of the same clade. *Antiviral Res, 176*, 104742.
689 doi:10.1016/j.antiviral.2020.104742
690 Daniloski, Z., Jordan, T. X., Wessels, H. H., Hoagland, D. A., Kasela, S., Legut, M., . . . Sanjana,
691 N. E. (2021). Identification of Required Host Factors for SARS-CoV-2 Infection in
692 Human Cells. *Cell, 184*(1), 92-105 e116. doi:10.1016/j.cell.2020.10.030
693 Davidson, A. D., Williamson, M. K., Lewis, S., Shoemark, D., Carroll, M. W., Heesom, K. J., . . .
694 Matthews, D. A. (2020). Characterisation of the transcriptome and proteome of
695 SARS-CoV-2 reveals a cell passage induced in-frame deletion of the furin-like
696 cleavage site from the spike glycoprotein. *Genome Med, 12*(1), 68.
697 doi:10.1186/s13073-020-00763-0
698 Gstraunthaler, G. (2003). Alternatives to the use of fetal bovine serum: Serum-free cell
699 culture. *Altex-Alternativen Zu Tierexperimenten, 20*(4), 275-281. Retrieved from <Go
700 to ISI>://WOS:000187567900005
701 Hadley, W. (2016). *Ggplot2*. New York, NY: Springer Science+Business Media, LLC.
702 Hoffmann, M., Kleine-Weber, H., & Pohlmann, S. (2020). A Multibasic Cleavage Site in the
703 Spike Protein of SARS-CoV-2 Is Essential for Infection of Human Lung Cells. *Mol Cell,*
704 *78*(4), 779-784 e775. doi:10.1016/j.molcel.2020.04.022

Hulswit, R. J., de Haan, C. A., & Bosch, B. J. (2016). Coronavirus Spike Protein and Tropism Changes. *Adv Virus Res, 96*, 29-57. doi:10.1016/bs.aivir.2016.08.004

Johnson, B. A., Xie, X., Kalveram, B., Lokugamage, K. G., Muruato, A., Zou, J., . . . Menachery, V. D. (2020). Furin Cleavage Site Is Key to SARS-CoV-2 Pathogenesis. *BioRxiv*. doi:10.1101/2020.08.26.268854

Katsura, H., Sontake, V., Tata, A., Kobayashi, Y., Edwards, C. E., Heaton, B. E., . . . Tata, P. R. (2020). Human Lung Stem Cell-Based Alveolospheres Provide Insights into SARS-CoV-2-Mediated Interferon Responses and Pneumocyte Dysfunction. *Cell Stem Cell*. doi:10.1016/j.stem.2020.10.005

Klimstra, W. B., Tilston-Lunel, N. L., Nambulli, S., Boslett, J., McMillen, C. M., Gilliland, T., . . . Duprex, W. P. (2020). SARS-CoV-2 growth, furin-cleavage-site adaptation and neutralization using serum from acutely infected hospitalized COVID-19 patients. *J Gen Virol, 101*(11), 1156-1169. doi:10.1099/jgv.0.001481

Lamers, M. M., Beumer, J., van der Vaart, J., Knoops, K., Puschhof, J., Breugem, T. I., . . . Clevers, H. (2020). SARS-CoV-2 productively infects human gut enterocytes. *Science*. doi:10.1126/science.abc1669

Lamers, M. M., van der Vaart, J., Knoops, K., Riesebosch, S., Breugem, T. I., Mykytyn, A. Z., . . . Haagmans, B. L. (2020). An organoid-derived bronchioalveolar model for SARS-CoV-2 infection of human alveolar type II-like cells. *EMBO J*, e105912. doi:10.15252/embj.2020105912

Lau, S. Y., Wang, P., Mok, B. W., Zhang, A. J., Chu, H., Lee, A. C., . . . Chen, H. (2020). Attenuated SARS-CoV-2 variants with deletions at the S1/S2 junction. *Emerg Microbes Infect, 9*(1), 837-842. doi:10.1080/22221751.2020.1756700

Liu, Z., Zheng, H., Lin, H., Li, M., Yuan, R., Peng, J., . . . Lu, J. (2020). Identification of Common Deletions in the Spike Protein of Severe Acute Respiratory Syndrome Coronavirus 2. *J Virol, 94*(17). doi:10.1128/JVI.00790-20

Millet, J. K., & Whittaker, G. R. (2015). Host cell proteases: Critical determinants of coronavirus tropism and pathogenesis. *Virus Res, 202*, 120-134. doi:10.1016/j.virusres.2014.11.021

Mykytyn, A. Z., Breugem, T. I., Riesebosch, S., Schipper, D., van den Doel, P. B., Rottier, R. J., . . . Haagmans, B. L. (2021). SARS-CoV-2 entry into human airway organoids is serine protease-mediated and facilitated by the multibasic cleavage site. *Elife, 10*. doi:10.7554/eLife.64508

Nikolic, M. Z., Caritg, O., Jeng, Q., Johnson, J. A., Sun, D., Howell, K. J., . . . Rawlins, E. L. (2017). Human embryonic lung epithelial tips are multipotent progenitors that can be expanded in vitro as long-term self-renewing organoids. *Elife, 6*. doi:10.7554/eLife.26575

Ogando, N. S., Dalebout, T. J., Zevenhoven-Dobbe, J. C., Limpens, R., van der Meer, Y., Caly, L., . . . Snijder, E. J. (2020). SARS-coronavirus-2 replication in Vero E6 cells: replication kinetics, rapid adaptation and cytopathology. *J Gen Virol*. doi:10.1099/jgv.0.001453

Osada, N., Kohara, A., Yamaji, T., Hirayama, N., Kasai, F., Sekizuka, T., . . . Hanada, K. (2014). The genome landscape of the african green monkey kidney-derived vero cell line. *DNA Res, 21*(6), 673-683. doi:10.1093/dnares/dsu029

Oude Munnink, B. B., Nieuwenhuijse, D. F., Stein, M., O'Toole, A., Haverkate, M., Mollers, M., . . . Dutch-Covid-19 response, t. (2020). Rapid SARS-CoV-2 whole-genome sequencing and analysis for informed public health decision-making in the Netherlands. *Nat Med, 26*(9), 1405-1410. doi:10.1038/s41591-020-0997-y

752 Rockx, B., Kuiken, T., Herfst, S., Bestebroer, T., Lamers, M. M., Oude Munnink, B. B., . . .
753 Haagmans, B. L. (2020). Comparative pathogenesis of COVID-19, MERS, and SARS in
754 a nonhuman primate model. *Science*. doi:10.1126/science.abb7314
755 Sachs, N., Papaspyropoulos, A., Zomer-van Ommen, D. D., Heo, I., Bottinger, L., Klay, D., . . .
756 Clevers, H. (2019). Long-term expanding human airway organoids for disease
757 modeling. *Embo j, 38*(4). doi:10.15252/embj.2018100300
758 Salahudeen, A. A., Choi, S. S., Rustagi, A., Zhu, J., van Unen, V., de la, O. S., . . . Kuo, C. J.
759 (2020). Progenitor identification and SARS-CoV-2 infection in human distal lung
760 organoids. *Nature*. doi:10.1038/s41586-020-3014-1
761 Sato, T., Vries, R. G., Snippert, H. J., van de Wetering, M., Barker, N., Stange, D. E., . . .
762 Clevers, H. (2009). Single Lgr5 stem cells build crypt-villus structures in vitro without
763 a mesenchymal niche. *Nature, 459*(7244), 262-265. doi:10.1038/nature07935
764 Shimomura, T., Ochiai, M., Kondo, J., & Morimoto, Y. (1992). A novel protease obtained
765 from FBS-containing culture supernatant, that processes single chain form
766 hepatocyte growth factor to two chain form in serum-free culture. *Cytotechnology,*
767 *8*(3), 219-229. doi:10.1007/BF02522039
768 Sutter, G., & Moss, B. (1992). Nonreplicating vaccinia vector efficiently expresses
769 recombinant genes. *Proc Natl Acad Sci U S A, 89*(22), 10847-10851.
770 doi:10.1073/pnas.89.22.10847
771 Tamura, D., Nguyen, H. T., Sleeman, K., Levine, M., Mishin, V. P., Yang, H., . . . Gubareva, L.
772 V. (2013). Cell culture-selected substitutions in influenza A(H3N2) neuraminidase
773 affect drug susceptibility assessment. *Antimicrob Agents Chemother, 57*(12), 6141-
774 6146. doi:10.1128/AAC.01364-13
775 Wei, H., Audet, J., Wong, G., He, S., Huang, X., Cutts, T., . . . Qiu, X. (2017). Deep-sequencing
776 of Marburg virus genome during sequential mouse passaging and cell-culture
777 adaptation reveals extensive changes over time. *Sci Rep, 7*(1), 3390.
778 doi:10.1038/s41598-017-03318-3
779 Wei, J., Alfajaro, M. M., Hanna, R. E., DeWeirdt, P. C., Strine, M. S., Lu-Culligan, W. J., . . .
780 Wilen, C. B. (2020). Genome-wide CRISPR screen reveals host genes that regulate
781 SARS-CoV-2 infection. *BioRxiv*. doi:10.1101/2020.06.16.155101
782 Wong, Y. C., Lau, S. Y., Wang To, K. K., Mok, B. W. Y., Li, X., Wang, P., . . . Chen, Z. (2020).
783 Natural transmission of bat-like SARS-CoV-2PRRA variants in COVID-19 patients. *Clin*
784 *Infect Dis*. doi:10.1093/cid/ciaa953
785 Youk, J., Kim, T., Evans, K. V., Jeong, Y. I., Hur, Y., Hong, S. P., . . . Lee, J. H. (2020). Three-
786 Dimensional Human Alveolar Stem Cell Culture Models Reveal Infection Response to
787 SARS-CoV-2. *Cell Stem Cell*. doi:10.1016/j.stem.2020.10.004
788 Zhou, J., Li, C., Liu, X., Chiu, M. C., Zhao, X., Wang, D., . . . Yuen, K. Y. (2020). Infection of bat
789 and human intestinal organoids by SARS-CoV-2. *Nat Med, 26*(7), 1077-1083.
790 doi:10.1038/s41591-020-0912-6
791 Zhu, N., Zhang, D., Wang, W., Li, X., Yang, B., Song, J., . . . Research, T. (2020). A Novel
792 Coronavirus from Patients with Pneumonia in China, 2019. *N Engl J Med, 382*(8),
793 727-733. doi:10.1056/NEJMoa2001017
794

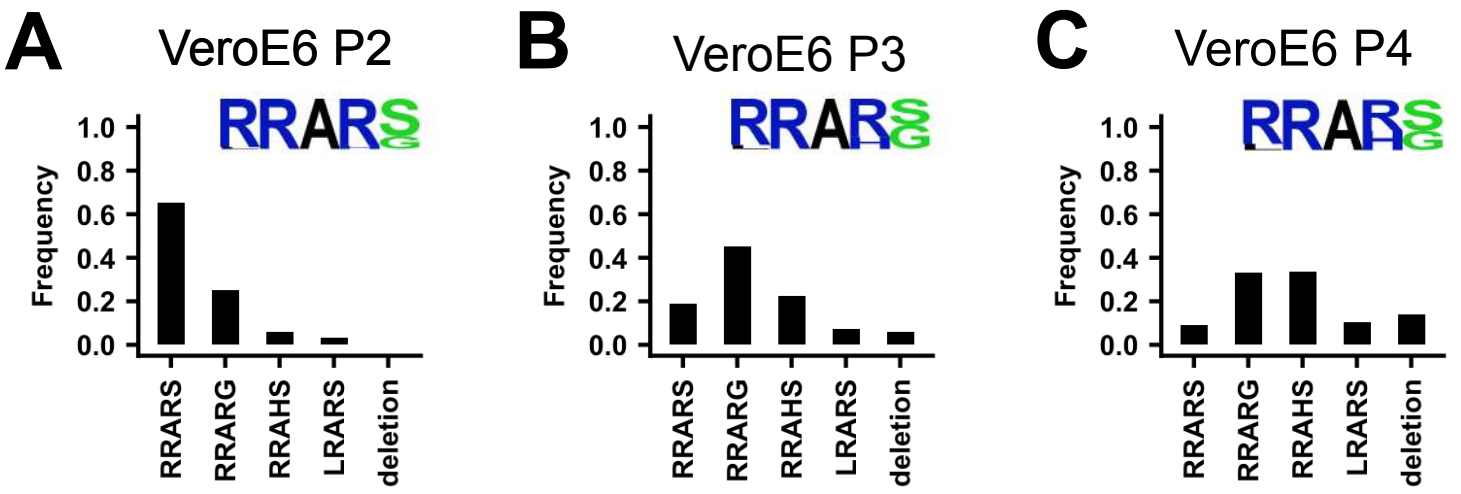

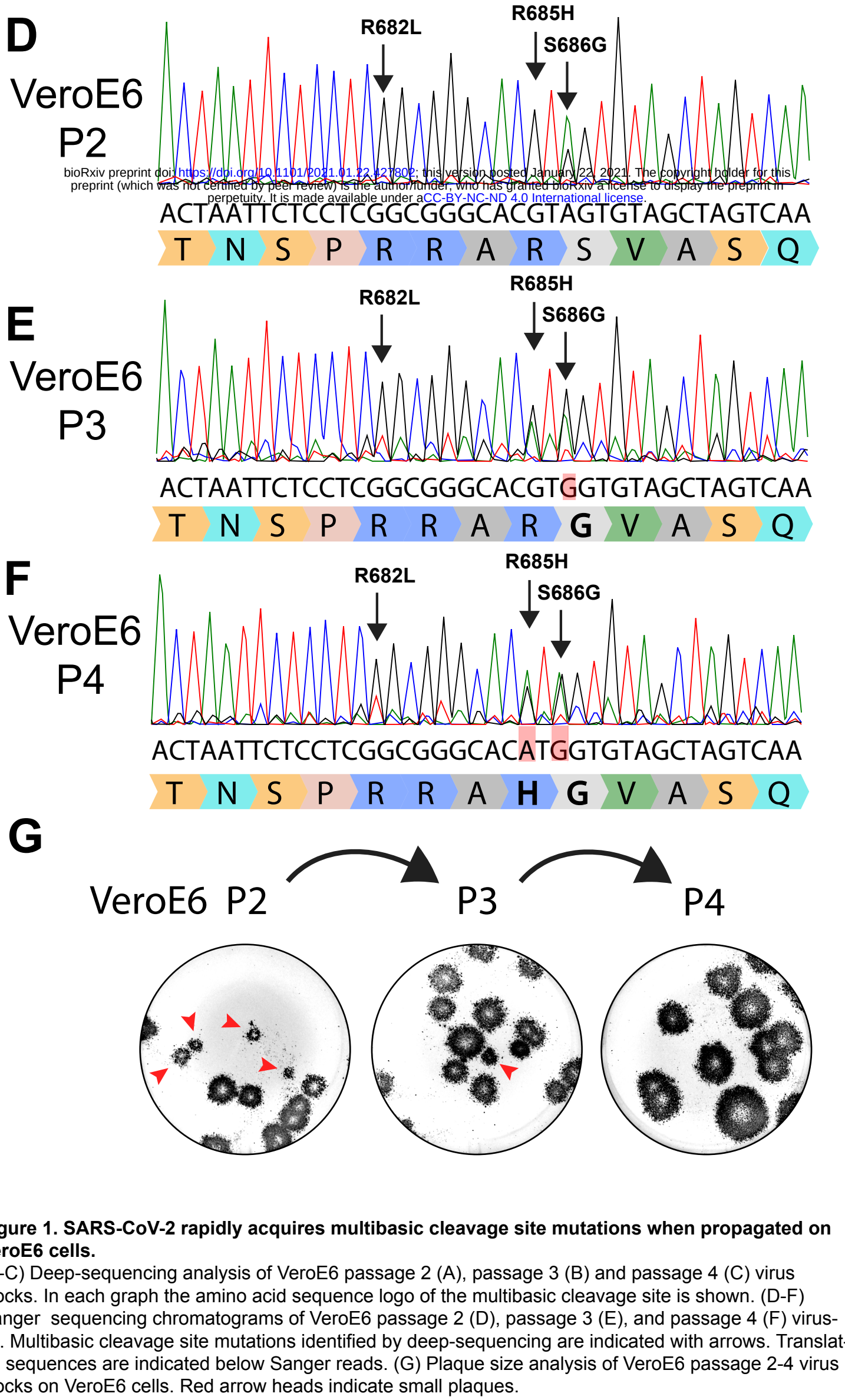

Figure 1. SARS-CoV-2 rapidly acquires multibasic cleavage site mutations when propagated on VeroE6 cells.
(A-C) Deep-sequencing analysis of VeroE6 passage 2 (A), passage 3 (B) and passage 4 (C) virus stocks. In each graph the amino acid sequence logo of the multibasic cleavage site is shown. (D-F) Sanger sequencing chromatograms of VeroE6 passage 2 (D), passage 3 (E), and passage 4 (F) viruses. Multibasic cleavage site mutations identified by deep-sequencing are indicated with arrows. Translated sequences are indicated below Sanger reads. (G) Plaque size analysis of VeroE6 passage 2-4 virus stocks on VeroE6 cells. Red arrow heads indicate small plaques.

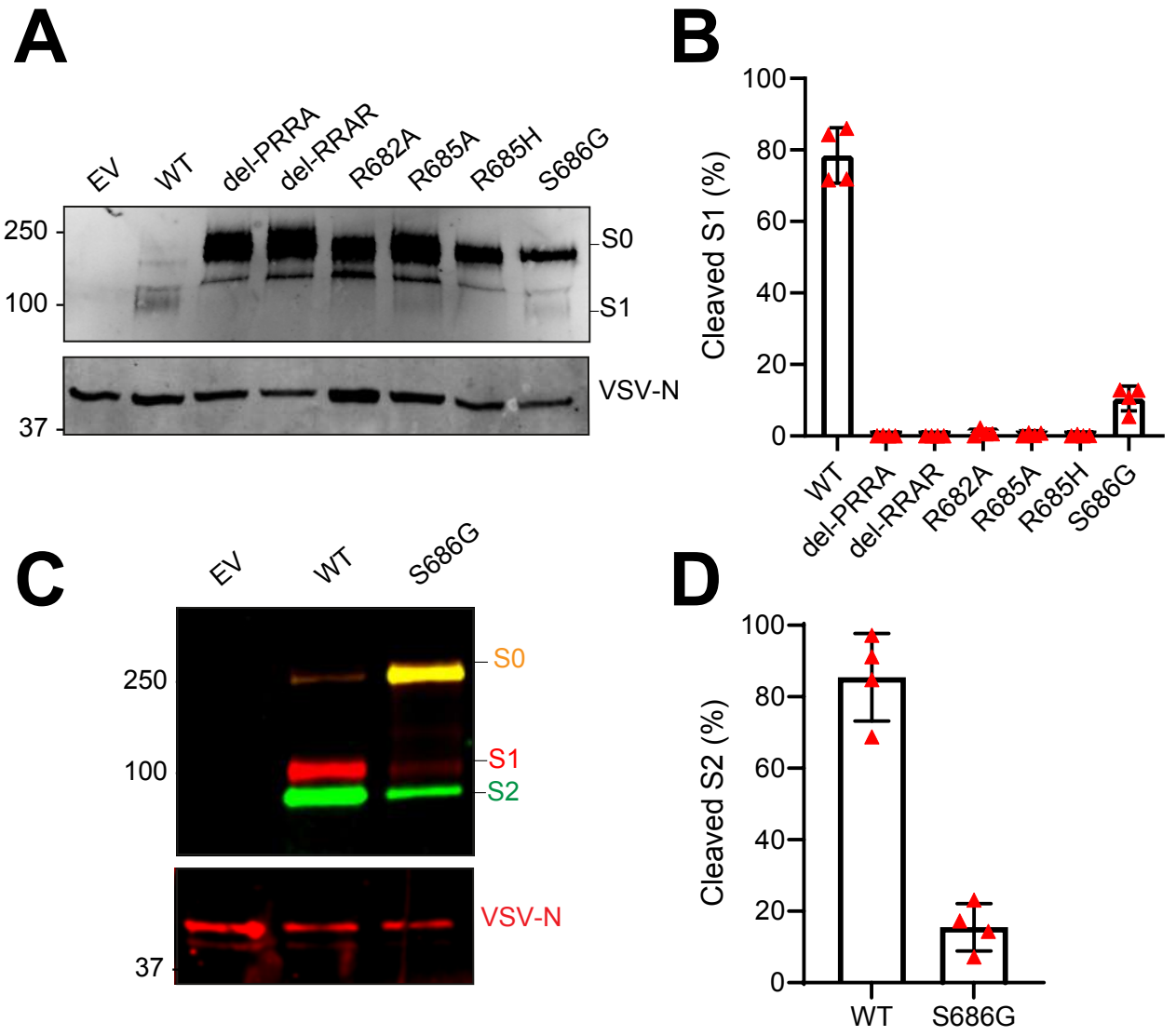

Figure 2. Mutations in the multibasic cleavage site and the adjacent serine residue (S686) abrogate S1/S2 cleavage. (A) Analysis of S1/S2 cleavage by S1 immunoblot of SARS-CoV-2 S (WT), multibasic cleavage site (MBCS) mutant and S686G mutant pseudoviruses. (B) Quantification of S1 cleavage from four independent pseudovirus productions. (C) Analysis of S1/S2 cleavage by multiplex S1 (red) and S2 (green) immunoblot of SARS-CoV-2 S (WT) and S686G mutant pseudoviruses. S0 indicates uncleaved spike; S1 indicates the S1 domain of cleaved spike; VSV-N indicates VSV nucleoprotein (production control). Numbers indicate the molecular weight (kDa) of bands of the protein standard. (D) Quantification of S2 cleavage from four independent pseudovirus productions. Error bars indicate SD. EV = empty vector. WT = wild type. kDa = kilo dalton.

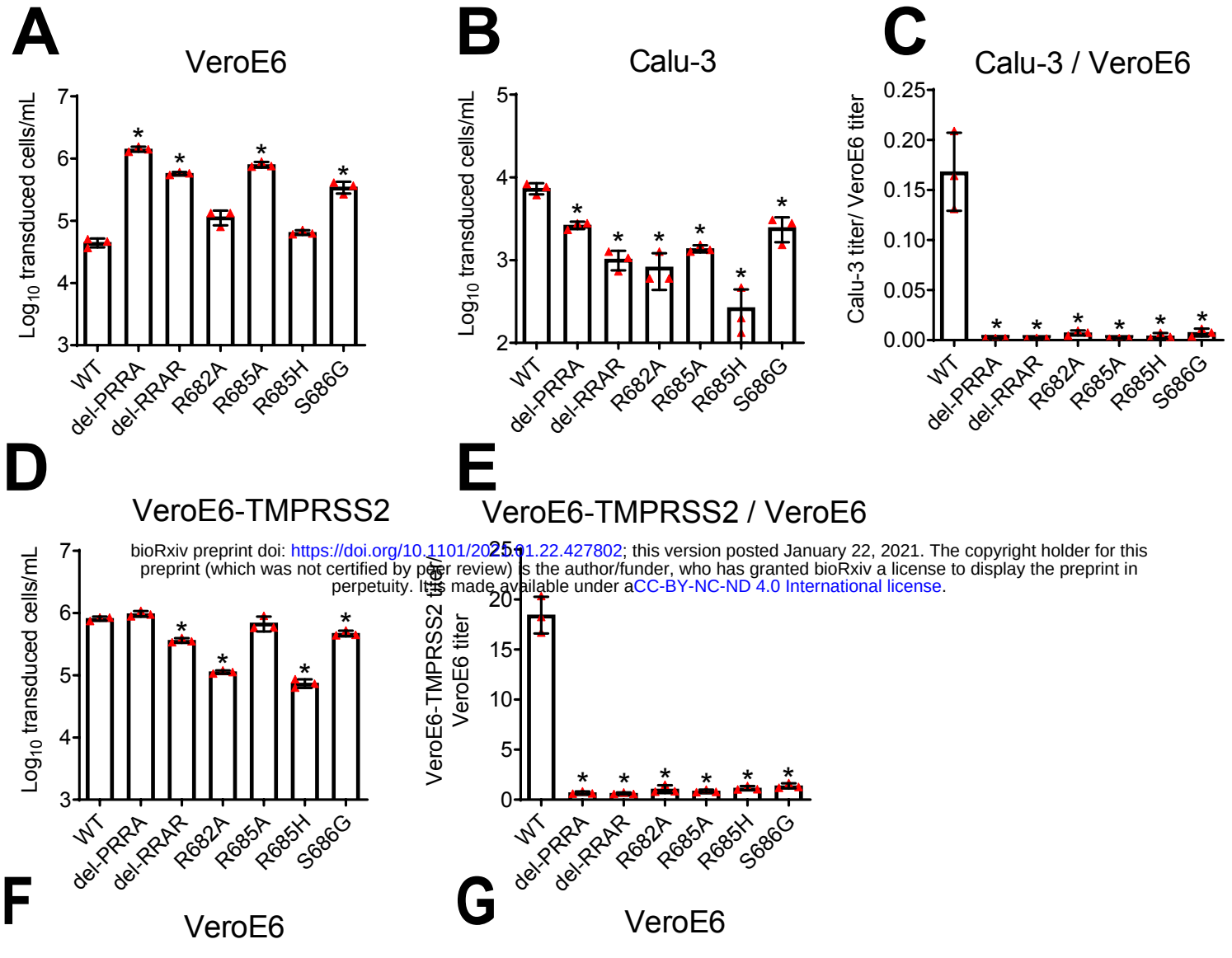

Figure 3. The SARS-CoV-2 multibasic cleavage site and the adjacent serine residue (S686) enhance infectivity and serine protease mediated entry on Calu-3 and VeroE6-TMPRSS2 cells. (A-B) SARS-CoV-2 (WT), multibasic cleavage site (MBCS) mutant and S686G pseudovirus infectious titers on (A) VeroE6 and (B) Calu-3 cells. (C) Fold change in SARS-CoV-2, MBCS mutant and S686G pseudovirus infectious titers on Calu-3 cells over infectious titers on VeroE6 cells. (D) SARS-CoV-2, MBCS mutant and S686G pseudovirus infectious titers on VeroE6-TMPRSS2 cells. (E) Fold change in SARS-CoV-2, MBCS mutant and S686G pseudovirus infectious titers on VeroE6-TMPRSS2 cells over infectious titers on VeroE6 cells. One-way ANOVA was performed for statistical analysis comparing all groups with WT. (F-I) SARS-CoV-2, MBCS mutant and S686G pseudovirus entry into (F and G) VeroE6 cells or (H and I) VeroE6-TMPRSS2 cells pre-treated with a concentration range of either (F and H) camostat mesylate or (G and I) E64D. Two-way ANOVA, followed by a bonferroni post hoc test was performed for statistical analysis comparing all groups to WT. WT pseudovirus entry into VeroE6 cells treated with 10μM E64D was significantly different from del-RRAR, R682A, R685A and S686G pseudovirus entry. * indicates statistical significance ($p<0.05$) compared to WT (A-E). * indicates statistical significance ($p<0.05$) compared to WT at the highest inhibitor concentration (F-I). Experiments were performed in triplicate. Representative experiments from at least two independent experiments are shown. Error bars indicate SD. WT = wild type.

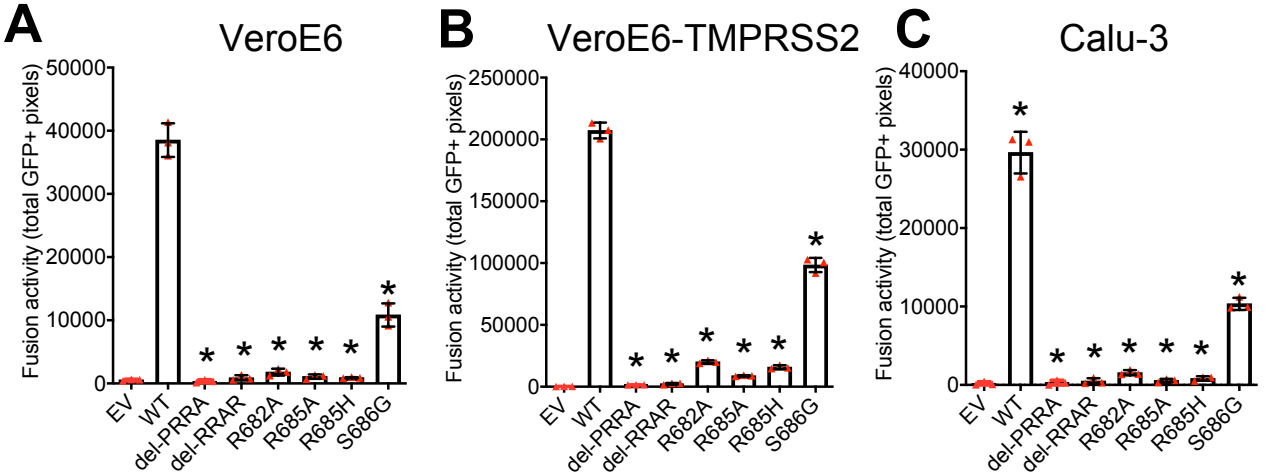

Figure 4. Multibasic cleavage site mutations and the adjacent serine residue (S686) impair spike protein fusogenicity.

(A-C) Fusogenicity of wild type SARS-CoV-2 spike and spike mutants was assessed after 18 hours by measuring the sum of all GFP+ pixels per well in a GFP-complementation fusion assay on VeroE6-GFP1-10 (A), VeroE6-TMPRSS2-GFP1-10 (B), and Calu-3-GFP1-10 (C) cells. The experiment was performed in triplicate. A representative experiment from two independent experiments is shown. Statistical analysis was performed by one-way ANOVA. * indicates a significant difference compared to WT ($P<0.05$). Error bars indicate SD. EV = empty vector. WT = wild type.

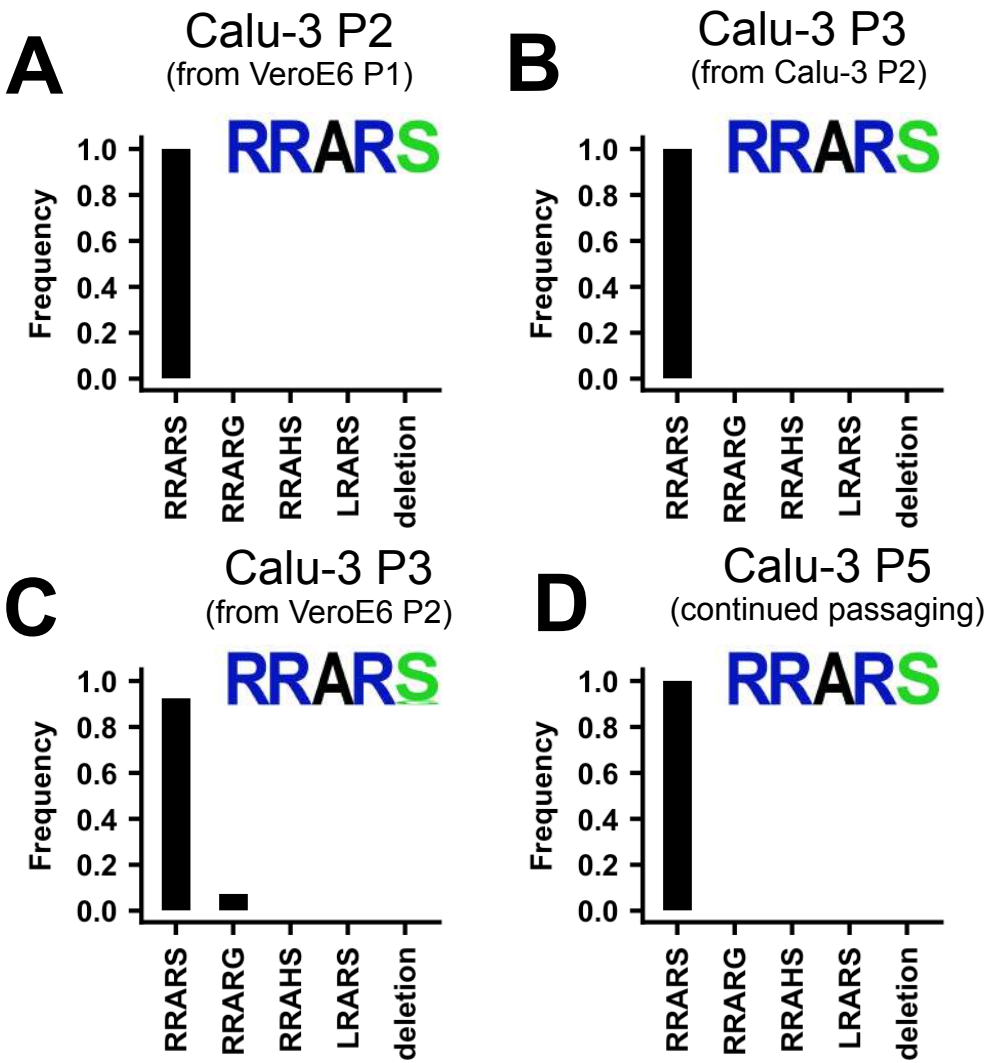

Figure 5. SARS-CoV-2 propagation in Calu-3 cells efficiently prevents SARS-CoV-2 cell culture adaptation.

(A) Deep-sequencing analysis of Calu-3 passage 2 virus from a VeroE6 passage 1. (B) Deep-sequencing analysis of Calu-3 passage 3 virus from the Calu-3 passage 2 in A. (C) Deep-sequencing analysis of Calu-3 passage 3 virus grown from a VeroE6 passage 2 stock (Figure 1A). Deep-sequencing analysis of Calu-3 passage 5 virus from a Calu-3 passage 3 stock in C. In each graph the amino acid sequence logo of the multibasic cleavage site is shown.

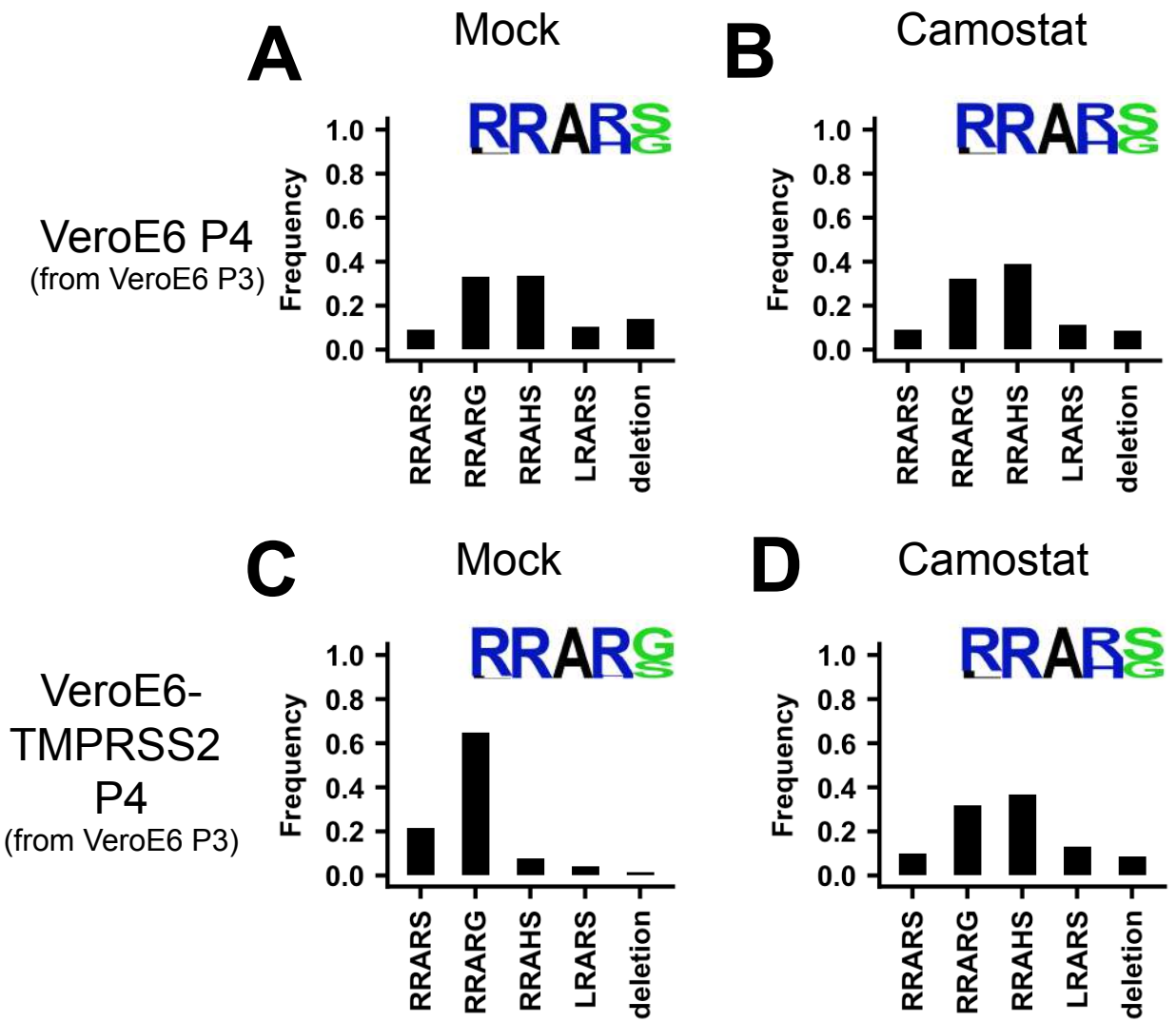

Figure 6. Serine protease expression prevents MBCS mutations.

(A-B) Deep-sequencing analysis of VeroE6 passage 4 virus from a VeroE6 passage 3 (A is a redisplay of Figure 1C) mock-treated or treated with 10μM Camostat. (C-D) Deep-sequencing analysis of VeroE6-TMPRSS2 passage 4 virus from a VeroE6 passage 3 mock-treated or treated with 10μM Camostat. In each graph the amino acid sequence logo of the multibasic cleavage site is shown.

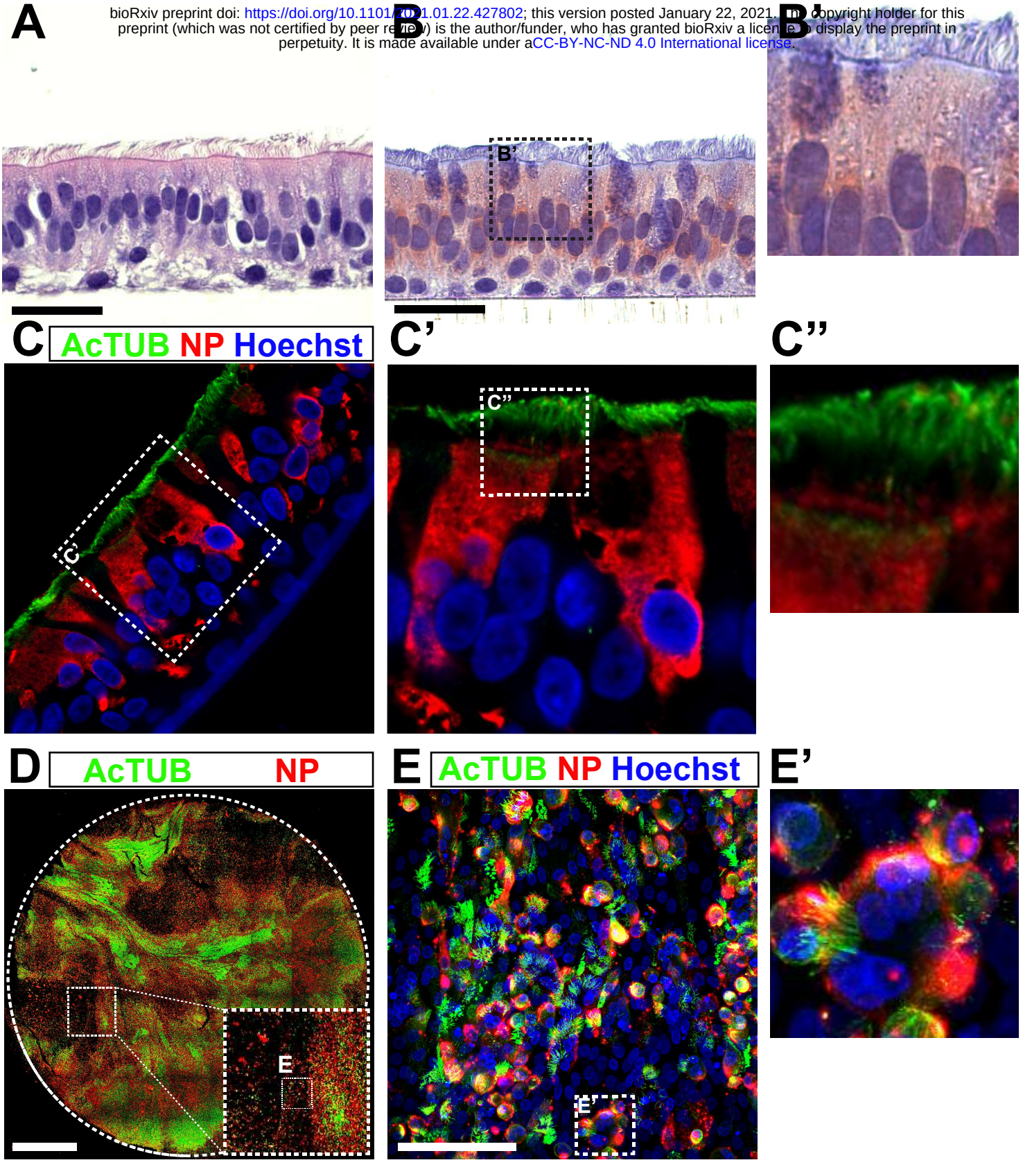

Figure 7. A 2D air-liquid interface human airway organoid model for SARS-CoV-2 propagation. (A) Human airway organoids were dissociated and plated onto 12 mm transwell inserts. After an 8-12 week differentiation period at air-liquid interface cultures contained ciliated, non-ciliated and basal cells as shown on a hematoxylin-eosin stain. (B) Air-exposed cells, but not basal cells, expressed the priming protease TMPRSS2 as shown by immunohistochemistry. (C) Immunofluorescent staining indicated that in these cultures, ciliated cells (acetylated tubulin+ or AcTUB+ cells) were infected by SARS-CoV-2. (D and E) At 5 days post-infection, whole-well confocal imaging indicated the infection was widespread (D) and cytopathic effects, including cilia damage (D and E) and syncytial cells (E) were visible. Scale bars indicate 20μm in A, B, C; 2mm in D; and 100μm in E.

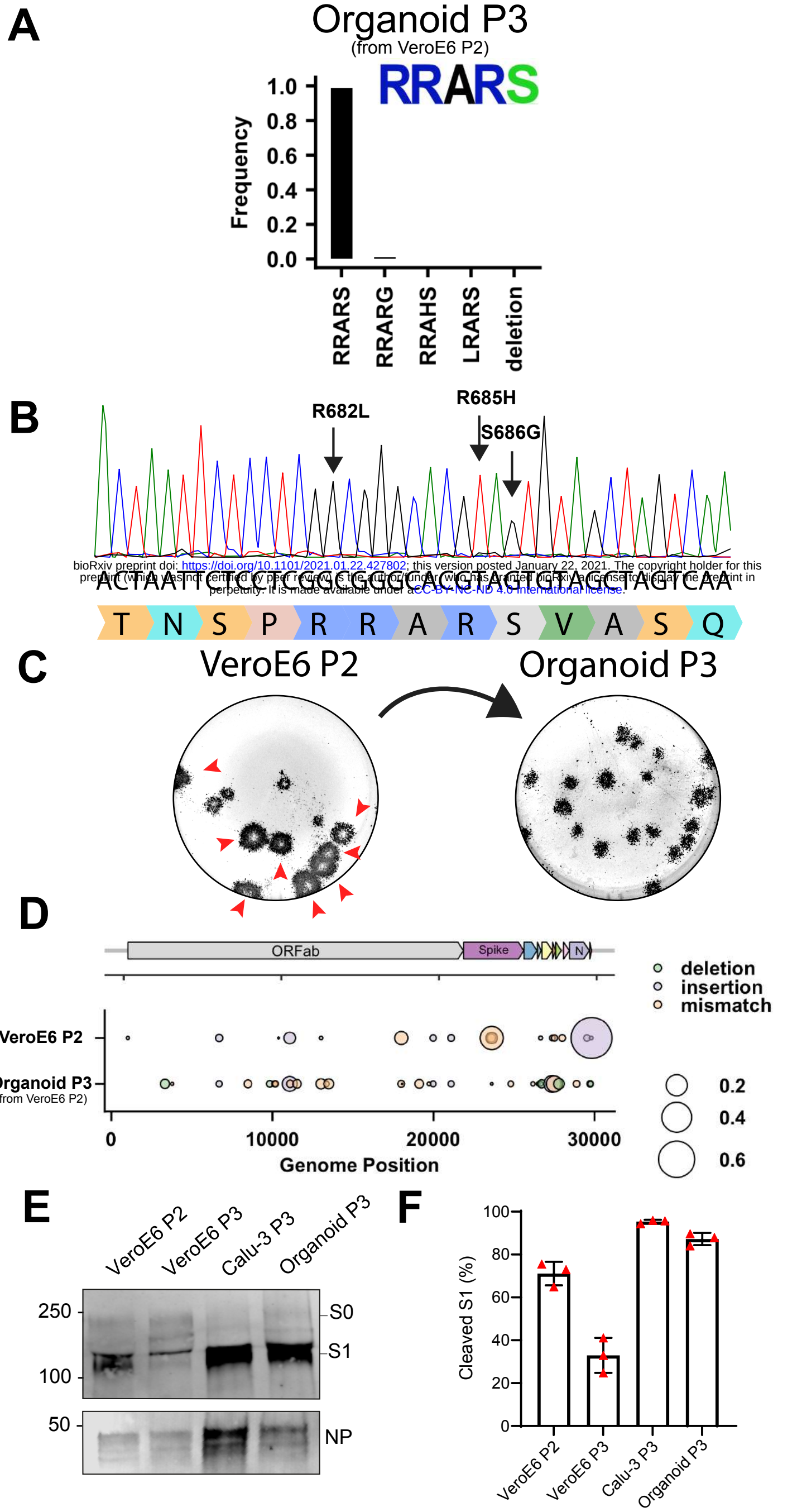

Figure 8. 2D air-liquid interface human airway organoids produce high titer stocks without multibasic cleavage site mutations.

(A-B) Deep-sequencing analysis (A) and Sanger chromatogram (B) of Organoid passage 3 virus from a VeroE6 passage 2 stock (Figure 1A). The amino acid sequence logo of the multibasic cleavage site is shown. The translated sequence is indicated below the Sanger read. Arrows indicate where cell culture adaptations to VeroE6 cells occur. (C) Plaque size analysis of VeroE6 passage 2 and Organoid passage 3 virus (the VeroE6 data is a redisplay of Figure 1G). Red arrow heads indicate large plaques. (D) Full genome deep-sequencing analysis of VeroE6 passage 2 and organoid passage 3 stocks. In D VeroE6 P2 is a redisplay of VeroE6 P2 in Figure supplement 1B. (E) Immunoblot analysis of VeroE6 passage 2 and 3, Calu-3 passage 3 and Organoid passage 3 stocks. S0 indicates uncleaved spike; S1 indicates the S1 domain of cleaved spike; NP indicates nucleoprotein. Numbers indicate the molecular weight (kDa) of bands of the protein standard. (F) Quantification of cleavage from three immunoblots. Error bars indicate SD. kDa = kilo dalton.

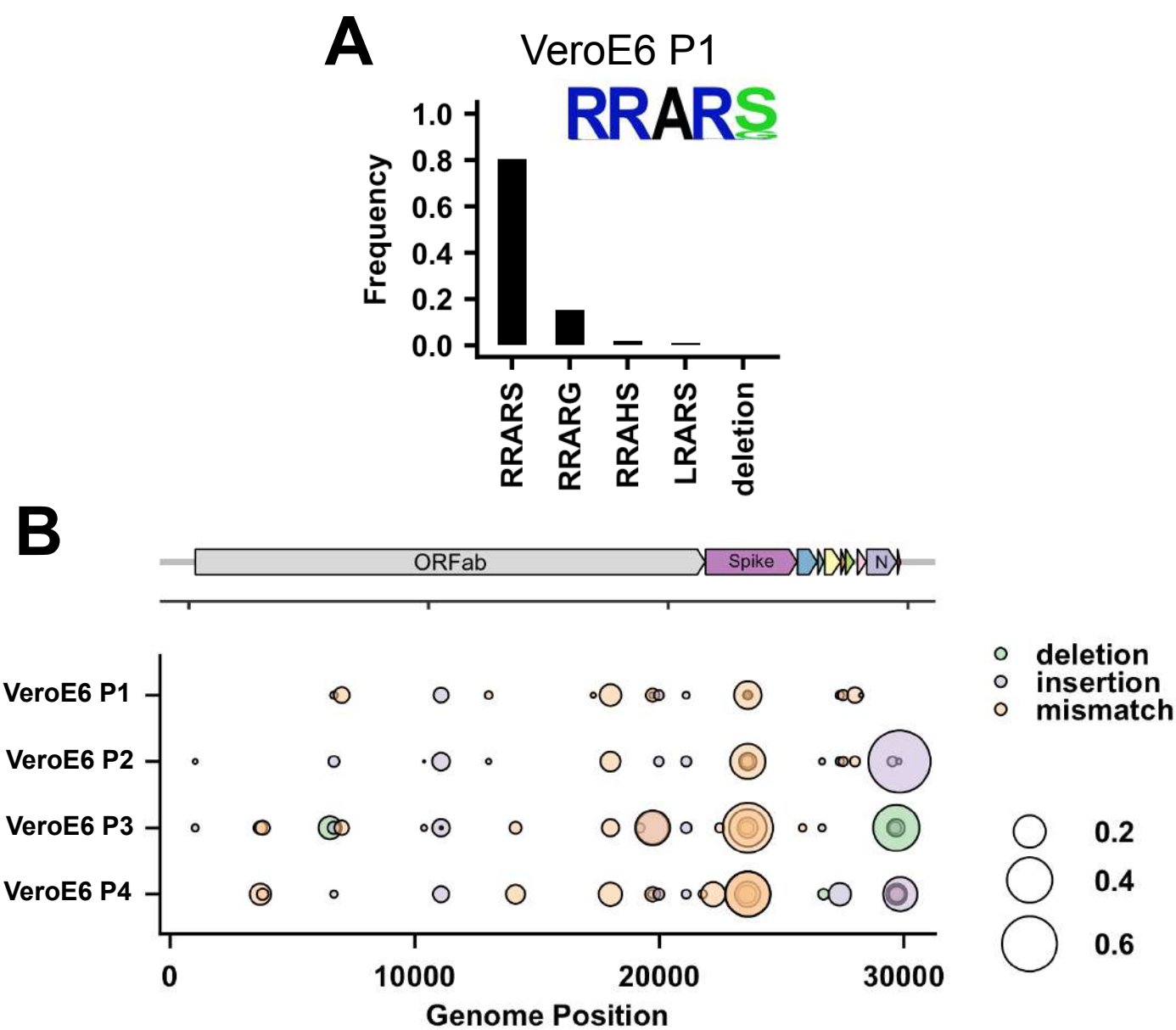

Figure supplement 1. Deep-sequencing analysis of VeroE6 passage 1 virus multibasic cleavage site and full genome deep-sequencing analysis of passage 1-4 viruses.
(A) Deep-sequencing analysis of the VeroE6 passage 1 virus stock. In each graph the amino acid sequence logo of the multibasic cleavage site is shown. (B) Full genome deep-sequencing analysis of VeroE6 passage 1, 2, 3 and passage 4 viruses.

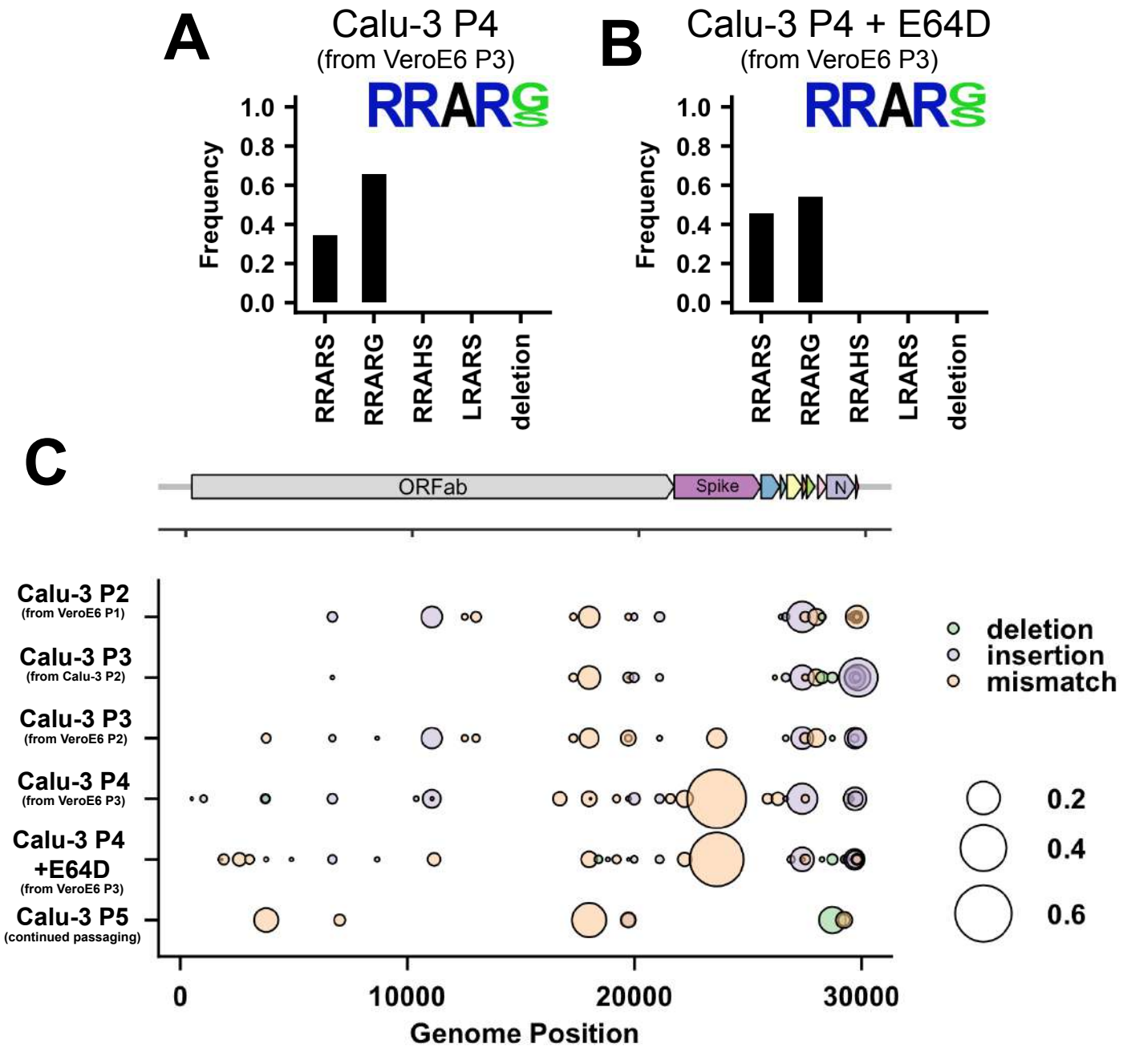

Figure supplement 5. Multibasic cleavage site deep-sequencing analysis of passage 4 Calu-3 viruses from an adapted VeroE6 P3 stock and full genome deep-sequencing analysis of Calu-3 propagated viruses.

(A) Deep-sequencing analysis of Calu-3 passage 4 virus from a VeroE6 passage 3 stock (from Figure 1B). (B) Deep-sequencing analysis of Calu-3 passage 4 virus from a VeroE6 passage 3 stock produced in the presence of 10μM E64D. In each graph the amino acid sequence logo of the multibasic cleavage site is shown. (C) Full genome deep-sequencing analysis of Calu-3 propagated viruses.

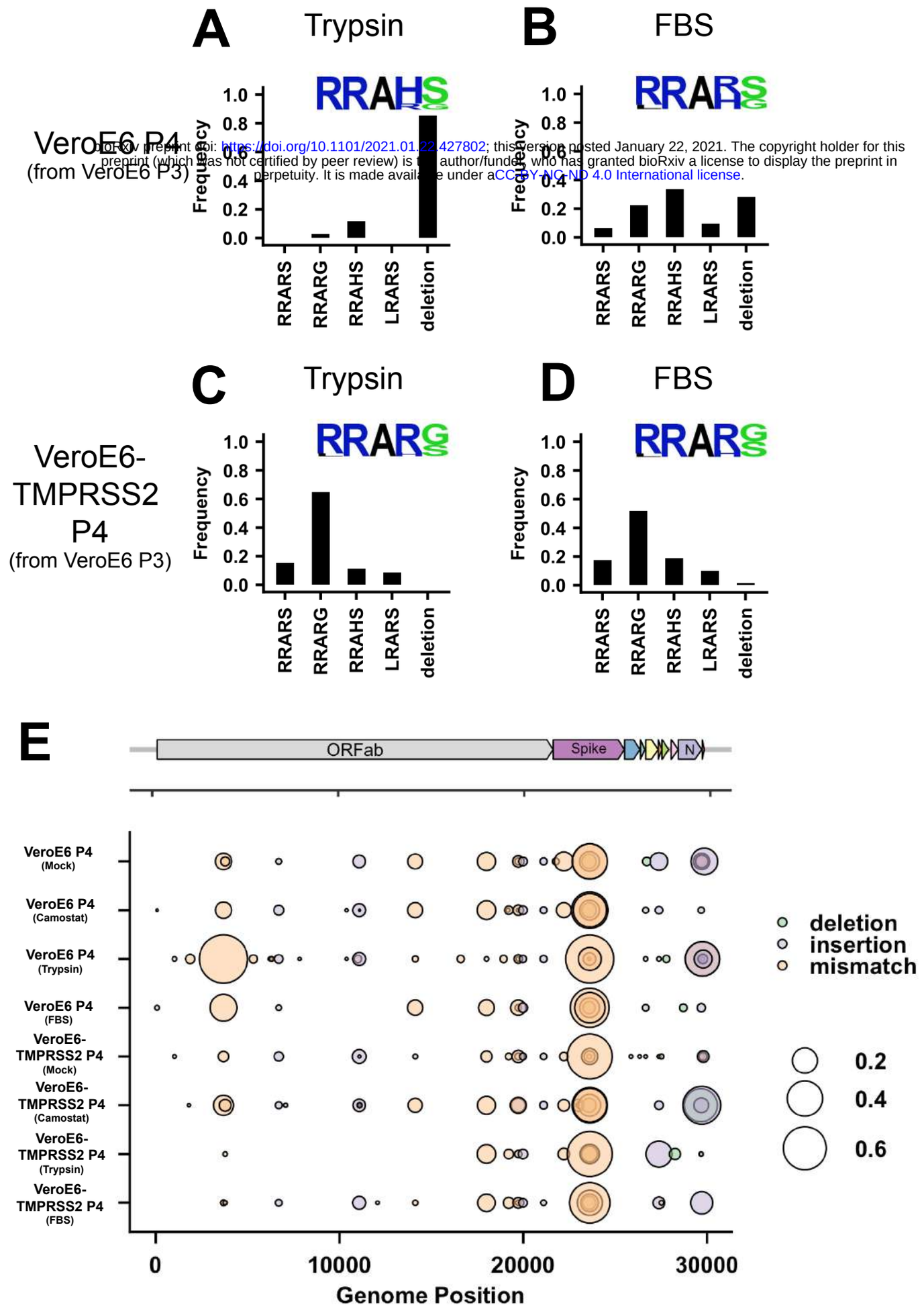

Figure supplement 6. Multibasic cleavage site and full genome deep-sequencing analysis of passage 4 VeroE6 and VeroE6-TMPRSS2 viruses.

(A-B) Deep-sequencing analysis of VeroE6 passage 4 virus from a VeroE6 passage 3, trypsin-treated (A) or treated with 10% FBS (B). (C-D) Deep-sequencing analysis of VeroE6-TMPRSS2 passage 4 virus from a VeroE6 passage 3, trypsin-treated (C) or treated with 10% FBS (D). In each graph the amino acid sequence logo of the multibasic cleavage site is shown. (E) Full genome deep-sequencing analysis of VeroE6 and VeroE6-TMPRSS2 propagated viruses. In E VeroE6 P4 (mock) is a redisplay of VeroE6 P4 in Figure supplement 1B.

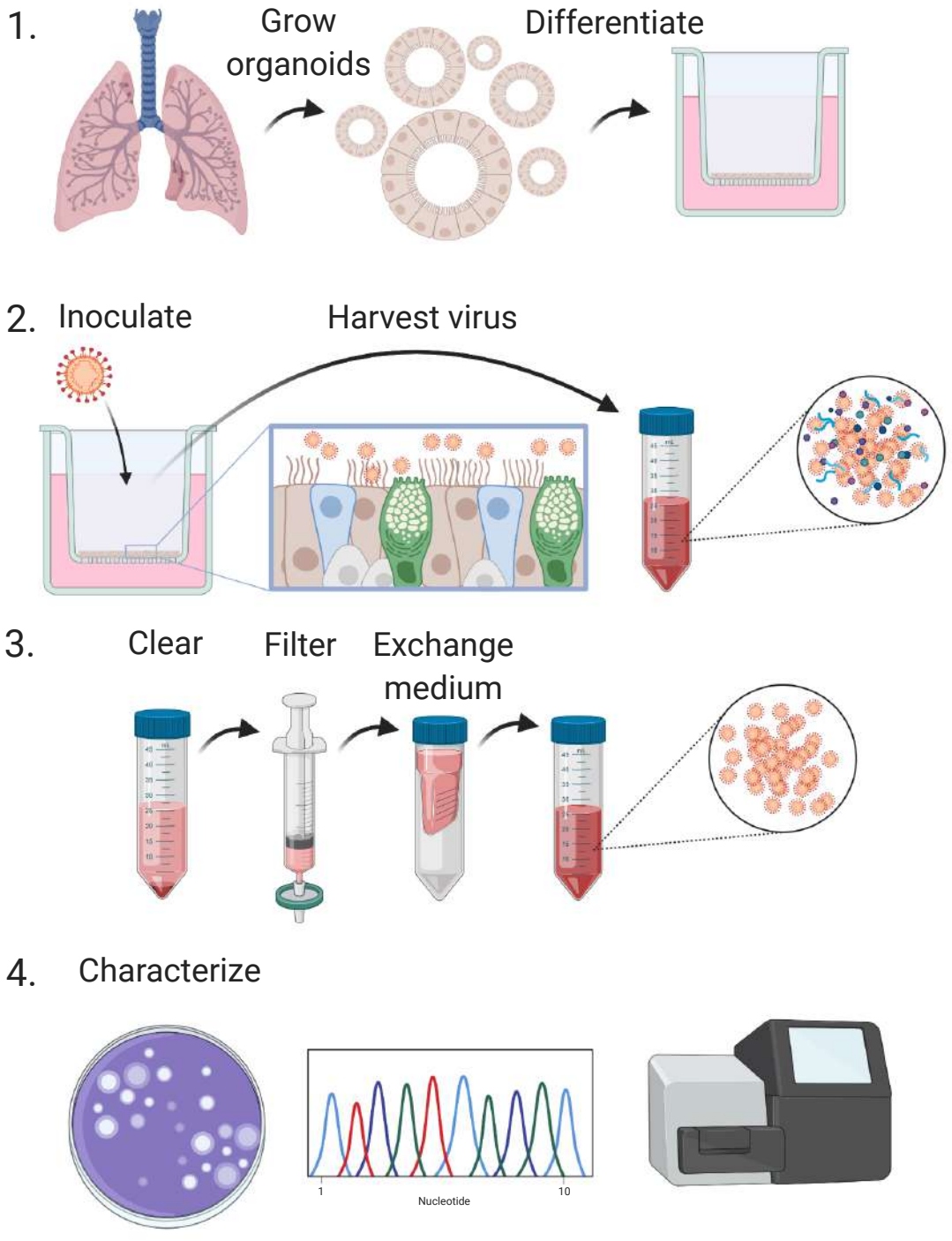

Figure supplement 8. Schematic workflow for the production of SARS-CoV-2 stocks on 2D air-liquid interface differentiated airway organoids.
Step 1. 3D self-renewing airway organoids are grown from human lung tissue. Next, these are dissociated to single cells and differentiated at air-liquid interface for 4-12 weeks.

Step 2. Differentiated cultures are infected at a multiplicity of infection of 0.05 and washed daily for 5 days. The washes from day 2-5 are collected and stored at 4°C.

Step 3. Virus collections are cleared by centrifugation and filtered to remove debris larger than 0.45 µm. Next, the medium is exchanged three times using Amicon columns to remove cytokines and debris smaller than 100 kDa. Purified virus preparations are then stored at -80°C in aliquots.

Step 4. Stocks can be characterized using plaque assays, Sanger sequencing and deep-sequencing. Created with BioRender.com.